Taylor & Francis
Taylor & Francis Group

Science and Technology of Advanced Materials

ISSN: 1468-6996 (Print) 1878-5514 (Online) Journal homepage: www.tandfonline.com/journals/tsta20

Recent advances in heteroatom-doped RuO_2 electrocatalysts for efficient acidic oxygen evolution reaction

Yihao Zheng, Tao Zhou, Quan Zhang, Haixin Guo, Jianxun Yang, Baofu Ding, Huaiyu Shao & Xinchun Yang

To cite this article: Yihao Zheng, Tao Zhou, Quan Zhang, Haixin Guo, Jianxun Yang, Baofu Ding, Huaiyu Shao & Xinchun Yang (18 Jun 2025): Recent advances in heteroatom-doped RuO_2 electrocatalysts for efficient acidic oxygen evolution reaction, Science and Technology of Advanced Materials, DOI: 10.1080/14686996.2025.2520159

To link to this article: https://doi.org/10.1080/14686996.2025.2520159

Publisher: Taylor & Francis & The Author(s). Published by National Institute for Materials Science inpartnership with Taylor & Francis Group.
Journal: *Science and Technology of Advanced Materials*

DOI: 10.1080/14686996.2025.2520159

Recent advances in heteroatom-doped RuO_2 electrocatalysts for efficient acidic oxygen evolution reaction

Yihao Zheng[a,b], Tao Zhou[b], Quan Zhang[c], Haixin Guo[d], Jianxun Yang[e], Baofu Ding[b,]*, Huaiyu Shao[a,]* and Xinchun Yang[b,]*

[a]Joint Key Laboratory of the Ministry of Education, Institute of Applied Physics and Materials Engineering, University of Macau, Avenida da Universidade, Taipa, Macao, 999078, China

[b]Institute of Technology for Carbon Neutrality, Shenzhen Institute of Advanced Technology, Chinese Academy of Sciences, Shenzhen 518055, China

[c]State Key Laboratory of Advanced Fiber Materials, College of Materials Science and Engineering, Donghua University, Shanghai 201620, China

[d]Agro-Environmental Protection Institute, Ministry of Agriculture and Rural Affairs, No. 31 Fukang Road, Nankai District, Tianjin 300191, China

[e]Three Gorges Daofu Renewables Co. Ltd, Ganzi 626700, China

CONTACT *E-mail address:* bf.ding@siat.ac.cn (B. Ding), hshao@um.edu.mo (H. Shao),

xc.yang@siat.ac.cn (X. Yang)

Abstract: Highly active and durable acidic oxygen evolution reaction (OER) electrocatalyst is a vital component of cost-effective proton exchange membrane water electrolyzer. Rutile-phase RuO_2 has inspired extensive attention as an acidic OER electrocatalyst due to its lower cost and similar activity compared to IrO_2. However, RuO_2 often suffers from severe dissolution and even structural collapse at high potentials due to the irreversible overoxidation of Ru into soluble RuO_4 species, resulting in a dramatic degradation of performance. Thus, suppressing Ru dissolution and improving intrinsic activity are crucial challenges in the design of RuO_2-based electrocatalysts. Extensive efforts have proven that incorporating foreign metal/non-metal dopants into RuO_2 is an extremely practical and effective strategy for boosting RuO_2. In this review, an overview of mechanisms of acidic OER and classification of the doping forms is first provided. Subsequently, a comprehensive review of RuO_2-based electrocatalysts with various doping types is presented, along with the underlying mechanisms that facilitate breaking the trade-off between activity and stability. Finally, our insights into current challenges and future research trends are proposed for developing robust RuO_2-based electrocatalysts toward acidic OER.

Keywords: electrocatalysis; acidic oxygen evolution reaction; RuO_2; heteroatom doping; proton exchange membrane water electrolyzer

The statement of novelty: This article systematically reviews the recent breakthroughs of the heteroatom-doped RuO_2 electrocatalysts based on a classification framework for doping strategies and presents the current challenges and the future opportunities.

1. Introduction

Hydrogen is regarded as a promising alternative for clean future due to its high energy density and harmless combustion products [1-3]. Currently, the source of hydrogen is primarily dependent on fossil fuel-based industrial production technologies with high carbon emissions [4, 5]. Water splitting powered by renewable energy is the most promising technology for hydrogen production with zero carbon emissions over the entire life cycle, and the resulting hydrogen is known as the green hydrogen [6-8]. The alkaline water electrolyzer (AWE) is the current dominant commercial hydrogen production technology, but suffers from poor dynamic responsiveness, low current density, and the risk of gas cross-permeation [9]. Compared to AWE, proton exchange membrane water electrolyzer (PEMWE) has significant advantages in the large-scale production of high-purity green hydrogen, due to its quick response, high proton conductivity, high energy conversion efficiency, and high safety [10]. However, the highly corrosive and oxidative operating environment at anode poses huge challenges to the durability of catalyst [11, 12], which hinders its industrial applications.

Water splitting mainly consists of the cathodic hydrogen evolution reaction (HER) and the anodic oxygen evolution reaction (OER) [13, 14]. The HER in the PEMWE is a simple reaction with rapid kinetics involving only two-electron transfer process, while the OER in the PEMWE is a complex multistep reaction with a sluggish four-electron transferred kinetics [15-17]. It is well-known that Ir-based catalysts are commonly used to catalyze OER in the PEMWE due to their sufficient acidic-corrosion resistance. However, their large-scale applications suffer from the extreme scarcity, high price, and relatively low activity [18-21]. In this regard, Ru-based catalysts, particularly rutile-phase RuO_2, have emerged as promising OER alternatives due to their exceptional intrinsic activity, favorable earth abundance, and cost-effectiveness [22, 23]. Nevertheless, their practical implementations face significant challenges in electrochemical [24, 25], particularly under high-potential conditions (>1.4 V vs.

RHE). This primarily stems from the oxidative dissolution of lattice oxygen, leading to the inevitable overoxidation of Ru into high-valence soluble RuO_4 species, and then the catastrophic structural disintegration [26-28]. To address such stability limitations, extensive investigations have focused on heteroelement doping strategies to engineer the rutile RuO_2 through tailoring the electronic configuration of Ru sites, stabilizing oxygen lattices, and optimizing intermediate adsorption energetics during the reaction pathways. Recent advancements have dramatically expanded the doping element spectrum, encompassing approximately 45% of the elements in the periodic table, with transition metals constituting the predominant category (Figure 1). Although numerous reviews related to Ru-based acidic OER electrocatalysts have been extensively reported, most of them reviewed a more comprehensive range of Ru-based catalysts including single atoms, alloys, oxides, heterostructures, and so on [24, 29-31]. To date, very few reviews have focused on the hot topic of heteroatom-doped RuO_2 electrocatalysts and provided systematic discussion and timely summary on different doping strategies. Thus, a review for summarizing such proliferation of doping investigations on RuO_2 is highly desirable.

Herein, we systematically summarize the recent breakthroughs of the heteroatom-doped rutile RuO_2-based electrocatalysts based on a classification framework for doping strategies, in particular, the fundamental mechanisms governing the acidic OER. We provide several representative examples to demonstrate the characteristics of the dopants located in different blocks, the effects and mechanisms of doping on performance, and the reaction pathways. Finally, we discuss the current challenges and the future opportunities. Our review aims to establish fundamental design principles bridging the gap between laboratory-scale catalyst innovation and industrial implementation of high-performance PEMWE systems.

2. Mechanisms of acidic OER

Generally, the acidic OER proceeds through three distinct mechanisms, including the adsorbate evolution mechanism (AEM), lattice oxygen mechanism (LOM), and oxide pathway mechanism (OPM). Each mechanism involves unique reaction pathways in terms of intermediate coordination chemistry, operando structural dynamics, and catalytic performance trade-offs, thus leading to complex stability-activity interdependence that necessitates atomic-level catalyst design.

AEM involves the stepwise conversion of surface adsorbed oxygen-containing intermediates (*OH, *O, *OOH) with four sequential proton-coupled electron transfer (PCET) steps, as illustrated in Figure 2a [29]. The mechanism initiates with H_2O molecule coordination at coordinatively unsaturated Ru sites, losing a proton to form *OH intermediates. Subsequently, *OH is deprotonated to form *O and reacted with another H_2O molecule to form *OOH intermediates, which was further deprotonated to generate *OO and ultimately release O_2. There is a well-established linear scaling relationship between the adsorption energies of *OH and *OOH intermediates, *i.e.*, $\Delta G_{*OOH} = \Delta G_{*OH} + 3.2 \pm 0.2$ eV, which leads to a minimum theoretical overpotential of approximately 370 mV for OER at standard conditions (25 ^{o}C, pH 0) [32]. Numerous reports have demonstrated that increasing the number of active sites and optimizing the adsorption energies of the intermediates (*OH, *O, *OOH) can increase the intrinsic activity of the catalysts and decrease the OER overpotential [33]. Additionally, the degradation of the catalyst can be suppressed due to the reduction of the required overpotential reaching the same current density.

The LOM represents a paradigm-shifting OER pathway that circumvents conventional *OOH intermediate formation through direct lattice oxygen participation in O−O bond formation, thus breaking the limitation of linear scaling relationship in the AEM and leading to a lower overpotential [34]. As illustrated in Figure 2b, the generation of *OH and *O intermediates in LOM follows the same pathway of AEM. The difference is that the *O intermediate can couple with neighboring lattice oxygen (O_L) to form an O−O bond and then release O_2, accompanied by the formation of an oxygen vacancy (O_V). Subsequently, the H_2O molecule can replenish the oxygen vacancy and recover the lattice oxygen sites. Similarly, lattice oxygen can also serve as initial adsorption sites, allowing direct coupling of the adsorbed *OH to lattice oxygen. In addition, direct O−O coupling of two adjacent lattice oxygen atoms may also occur in the OER process [35]. Although the reaction energy barrier is lowered in LOM due to the participation of lattice oxygen, the excessive loss of lattice oxygen may induce the structural degradation of the catalyst [36]. Thus, the trade-off between enhanced activity and inherent stability of RuO_2 catalysts were achieved by decreasing the orbital hybridization of Ru 4*d*-O 2*p* and then weakening the Ru−O covalency, thus inhibiting the lattice oxygen participation [37].

The main feature of the OPM is the direct coupling of two *O intermediates at the bimetallic active sites to form O_2 without *OOH formation and lattice oxygen participation, thus boosting both activity and stability [38]. As illustrated in Figure 2c, *O intermediates are first generated at two adjacent metal active sites, and subsequent the *O intermediates are directly coupled to form O−O bonds and then release O_2. The OPM usually occurs on the specific bimetallic sites with shortened interatomic distances and enhanced *OH adsorption to promote *O intermediates generation [39].

3. Evaluation of acidic OER electrocatalysts

For the performance evaluation of acidic OER electrocatalysts, activity and stability are the two main aspects [6]. Catalytic activity is usually evaluated by overpotential (η), Tafel slope, charge transfer resistance (R_{ct}), electrochemically active surface area (ECSA), specific activity, mass activity (MA), turnover frequency (TOF), Faradaic efficiency, and other indicators. Stability tests are generally performed by chronopotentiometry (CP), chronoamperometry (CA), and accelerated durability test (ADT). In addition, the precious metal dissolution rate can be calculated from the inductively coupled plasma (ICP) results after stability tests. For structural characterization and mechanism verification, transmission electron microscopy (TEM), X-ray diffraction (XRD), differential electrochemical mass spectrometry (DEMS), and in situ/non in situ spectroscopic analyses including X-ray absorption spectroscopy (XAS), X-ray photoelectron spectroscopy (XPS), Raman spectroscopy, and Fourier transform-infrared (FT-IR) spectroscopy are commonly adopted [1].

4. Classification of doping forms for RuO_2

Heteroatom doping in rutile RuO_2 manifests through two primary crystallographic configurations: substitutional and interstitial doping. As illustrated in Figure 3, substitutional doping occurs through either cationic replacement – heteroatoms occupying Ru lattice sites

(Figure 3a) [40], or anionic substitution – non-metal elements replacing oxygen sublattice positions, significantly altering metal-oxygen covalency and redox potentials (Figure 3b) [41]. Interstitial doping introduces heteroatoms into octahedral voids of the rutile framework (Figure 3c) [42], preferentially occurring in low-coordination surface regions. In addition, these fundamental modes have derived a series of advanced doping architectures, including cooperative (Co)-doping systems (*e.g.*, cation-anion dual doping) [43], solid solutions (*e.g.*, cation substitution with tunable stoichiometric ratios) [44], and surface-anchored complexes (*e.g.*, sulfate functionalization) [45].

5. Doping strategies for RuO_2-based electrocatalysts

Current advancements in RuO_2 catalyst engineering have established a diversified doping library spanning over 45 elements across the periodic table (Figure 1), based on the five strategic approaches, including cation doping, anion doping, cation-anion dual doping, interstitial doping, and solid solution oxides. The data related to the activity and stability of various catalysts are shown in Table 1.

5.1. Cation doping

Cation doping is a common and effective strategy to regulate the electronic structure of RuO_2, thereby improving its activity and stability. Various metal elements are incorporated into the RuO_2 matrix in the form of monodoping or co-doping, where metal dopants can substitute the lattice position of Ru in the RuO_2. Differences in the oxidation state of the cation, the lattice parameters of the corresponding oxide, and the doping concentration will lead to changes in structure and catalytic performance.

5.1.1. Monodoping

s-block metals. The metal elements in the s-block, including Na, Mg, Ca, Ba, etc., have been used as dopants of RuO_2-based catalysts [46-49, 124]. Since the corresponding ionic valences of these elements are lower than Ru^{4+} ion, in order to maintain charge neutrality, oxygen vacancies could be generated when Ru^{4+} ions are substituted by the lower valence-state ions. The presence of oxygen vacancies can regulate the geometric and electronic structure of RuO_2, thus affecting catalytic activity and stability. Zhang et al. engineered a novel Na-doped RuO_2

catalyst featuring an amorphous/crystalline heterostructure with tailored oxygen vacancies and interfacial grain boundaries (Figure 4a,b) [47]. The multiscale defect architecture endows the a/c-RuO_2 with exceptional stability under harsh corrosive and oxidative conditions. Density functional theory (DFT) calculations indicated that the enhanced activity originates from the synergistic downshift of the *d*-band center of Ru sites by the Na dopants and oxygen vacancies (Figure 4), weakening oxygen intermediate adsorption strengths, thereby lowering the energy barrier for the rate-determining OER step (Figure 4d). The Ca-doped RuO_2 was prepared by a molten salt method [124], where Ca^{2+} ions functioned as structural modifiers to introduce oxygen vacancy formation during subsequent electrochemical activation, yielding oxygen vacancy-rich RuO_2 nanoparticles (RuO_2-O_V). The introduced oxygen vacancies distorted the local RuO_6 octahedron symmetry, causing the upward shift in the Ru *d*-band center and the decreased covalency of Ru−O. This electronic reconfiguration optimized the adsorption of oxygen intermediates, suppressed the dissolution of Ru through improved metal-oxygen charge transfer, and thus, boosted both catalytic activity and operational stability.

d-block metals. Transition metal elements in the d-block often exhibit multiple variable valence states due to the participation of *d*-orbital electrons in bonding. The electronic structure of Ru can be modulated by lattice doping of transition metal elements with different valence states and electronegativity, resulting in the optimization of adsorption and desorption of oxygen intermediates. The doping of transition metals in the d-block can be divided into two parts: non-precious transition metal and precious metal doping. Non-precious transition metals in the d-block such as first-row transition metals (V, Cr, Mn, Ni, Cu, Zn, etc.) have been corroborated to be effective single dopants [40, 53-56, 59, 63-67]. It was found that the OER kinetics could be improved by the interaction between Cr dopants and Ru, by which a Cr-mediated OH spillover occurred from Cr site to the adjacent Ru site to generate *OOH (Figure 4e), resulting in a rate-limiting step transition from *OOH generation to O_2 generation (Figure 4f) [54]. Thus, $Cr_{0.2}Ru_{0.8}O_{2-x}$ demonstrated boosted OER activity with an ultralow overpotential of only 170 mV at 10 mA cm^{-2}. This suggests that dopant-mediated OH spillover is an effective strategy to enhance the activity of RuO_2. The deactivation of Ru site in RuO_2 is mainly caused by two aspects: overoxidation and dissolution of Ru caused by lattice oxygen oxidation and direct demetallation of the surface unsaturated Ru site [11, 125]. It was found that the incorporation of Ni to the lattice of RuO_2 could stabilize subsurface oxygen and surface Ru through increasing the energies cost for structural degradation (Figure 4g), thereby contributing to much improved structural stability of Ru site during acidic OER [59]. As a result, the resulting Ni-RuO_2 catalyst was coupled with a commercial Pt/C catalyst to assemble a PEM electrolyzer, showing exceptional stability during >1000 h of operation at 200 mA cm^{-2}. Qin et al. introduced V single atoms and oxygen-bridged V dimers into RuO_2 to synthesize a two-dimensional RuO_2 catalyst with highly asymmetric Ru−O−V local structure (Figure 5a) [63]. The strong interaction of the Ru−O−V local structure shortened the distance between Ru and V site (Figure 5b), thus altering the OER pathway from conventional AEM to oxygen radical coupling mechanism (OCM) (Figure 5c). Meanwhile, Ru−O−V local structure reduced the valence state of Ru and inhibited the overoxidation of Ru. The V_n−RuO_2 showed much improved stability of 1050 h at 10 mA cm^{-2} with a slow degradation of 0.12 mV h^{-1} in 0.1 M $HClO_4$. Mn is also a great dopant to improve the activity and stability of RuO_2. Zhao et al. found that the synergistic strategy of Mn doping and hydroxylation can stabilize Ru active site and lattice oxygen and reduce the energy barrier of the rate-determining step from *O to *OOH for the AEM pathway, thus improving the stability and activity of RuO_2. In addition, Cu-doped RuO_2 can be synthesized by an ion exchange reaction of Ru^{3+} and Cu-BTC (a metal-organic framework, MOF) and subsequent annealing of Ru-exchanged Cu-BTC [40]. The doping of low-valent Cu promoted the generation of oxygen vacancies, which in turn induced the formation of unsaturated Ru sites in the near vicinity. DFT calculations revealed the high-index facets containing low-coordination unsaturated Ru sites contributed more catalytic activity to OER and highlighted the crucial roles of Cu dopants in regulating surface electronic structure and inducing the formation of unsaturated Ru sites. Like Cu^{2+}, the doping of Zn^{2+} also can lead to the formation of oxygen vacancies. Zhang et al. reported that a synergistic strategy of Zn doping and oxygen vacancy (Figure 5d) optimized the adsorption of oxygen intermediates on Ru and Zn sites, resulting in the alteration of the OER pathway from AEM to OPM [65]. The OPM pathway could bypass the formation of *OOH intermediates, reduce the reaction energy barrier, and inhibit the overoxidation of Ru sites. As a result, the as-prepared py-RuO_2:Zn showed excellent OER performance with overpotentials of 173, 304, and 373 mV to deliver current densities of 10, 500, 1000 mA cm^{-2} (Figure 5e), respectively, and exceptional stability for 1000 h at 10 mA cm^{-2} (Figure 5f).

The reports have convinced the doping of high-valence transition metals (Nb, Mo, Ta, Re) can stabilize Ru active sites [57, 58, 60-62]. For example, the Ru−O−Nb structure generated by Nb doping can reduce the OER barrier and prevent overoxidation of Ru sites through electron transfer from Nb to Ru (Figure 6a-c) [58]. It is worth mentioning that the resultant $Nb_{0.1}Ru_{0.9}O_2$ exhibited excellent stability for 360-h test at 200 mA cm^{-2} with a degradation rate of only 25 μV h^{-1}. Zhang et al. found that structure-dependent corrosion of RuO_2 was responsible for Ru dissolution by studying well-defined RuO_2 surfaces with selected crystal orientations [62]. It was demonstrated that the incorporation of Ta dopant could both inhibit the corrosion of RuO_2 and improve the activity of RuO_2. Impressively, in an industrial-scale PEMWE, the extraordinary durability of $Ta_{0.1}Ru_{0.9}O_{2-x}$ was shown during 2800 h at 1 A cm^{-2} with a degradation rate of only 14 μV h^{-1}. The charge transfer between traditional dopants and Ru sites is essentially static charge redistribution, which has certain limitations for simultaneously elevating both activity and stability due to the unidirectional form of electron transfer within catalyst. Re dopants with multiple valence states can offer a dynamic electron accepting-donating for Ru active sites [60]. On one hand, Re dopants accepted electrons from Ru to improve the oxidation state of Ru sites to boost catalytic activity at low potential. On the other hand, Re dopants served as the electron donor to give electrons to suppress the overoxidation of Ru sites at large potential (Figure 6g). It was verified that the dynamic electron interaction altered the OER pathway from LOM to AEM and reduced the activation energy barrier from *O to *OOH intermediates, enabling both high activity and durability of Re-doped RuO_2.

Doping of noble metal Rh and Ir into RuO_2 can also significantly improve the activity and stability for OER [50-52]. Wang et al. introduced low-valent Rh into RuO_2 on graphene, accompanied by the generation of oxygen vacancies [50]. The synergistic strategy of Rh doping and oxygen vacancy enabled a more optimal reaction pathway of lattice oxygen mediated mechanism-oxygen vacancy site mechanism (LOM-OVSM). This unconventional OER mechanism with the rate-determining step of *O generation broke the limitation of the reaction energy barrier of *OOH formation for AEM. The reversible oxygen vacancies (Figure 7a,b) were responsible for much improved catalytic activity and stability of Rh-RuO_2/G. The Rh-RuO_2/G showed an overpotential of 161 mV to deliver a current density of 10 mA cm^{-2}, together with great stability over 700 h at 50 mA cm^{-2}. Wu et al. introduced Ru–O–Ir atomic interfaces into RuO_2 through a thermal-driven cation exchange strategy [51]. The bridging oxygen site at the Ru–O–Ir atomic interface served as a proton acceptor to capture proton from the adjacent Ru site and facilitate the deprotonation of oxygen intermediates (Figure 7c). The construction of Ru–O–Ir atomic interfaces broke the limitation of linear scaling relationship between the adsorption energy of *OH and *OOH and inhibited the overoxidation of Ru sites to higher oxidation states. The Ir-RuO_2 catalyst delivered the current densities of 10 and 1500 mA cm^{-2} at low overpotentials (Figure 7d) of 167 and 390 mV and maintained good stability during operation exceeding 1000 h at 10 mA cm^{-2}. Notably, the PEMWE using Ir-RuO_2 as the anode catalyst needed merely 1.6 V and 1.8 V to achieve current densities of 1 and 2 A cm^{-2}, respectively, and operated steadily at 1 A cm^{-2} for 300 h.

f-block metals. Rare earth metals (La, Ce, Nd, Sm, Er) located in the f-block have been demonstrated to be effective dopants to alter the OER activity and stability of RuO_2 by doping them into the lattice of RuO_2 [69-75]. Zhang et al reported a La-doped RuO_2 supported on titanium mesh (La-RuO_2@TM) [72]. The La−O−Ru local structure formed by La doping significantly optimized the adsorption energies of the oxygen intermediates and then lowered the reaction barrier of the rate-determining step. It was found that the electron transfer from La to Ru reduced the oxidation state of Ru and significantly inhibited the overoxidation of Ru. Accordingly, the catalytic activity and stability of La-RuO_2@TM were dramatically improved toward acidic OER. It is acknowledged that Ru−O covalency plays a significant role in regulating the structural stability of RuO_2. Both excessively weak and strong Ru−O covalency may lead to instability and even inactivation of Ru sites. However, precisely and continuously regulating Ru−O covalency is difficult for transition metal dopants with *d*-valence electrons. Li et al. introduced lanthanide elements with gradient-filled 4*f* electrons into RuO_2 to precisely tune Ru−O covalency [71]. Through theoretical calculations, the Er-RuO_x with the optimal Ru−O covalency was screened out due to its highest formation energy of Ru and O vacancies compared with Ho-RuO_x, and Tm-RuO_x, RuO_2 (Figure 8a,b). Thus, the Er-RuO_x showed exceptional stability that is 35.5 times higher than commercial RuO_2. The PWMWE composed of Er-RuO_x and Pt/C realized voltages as low as 1.590, 1.713, and 1.837 V at 1, 2, 3 A cm^{-2} (Figure 8c), and showed excellent durability at 500 mA cm^{-2} with a degradation rate of only 37 μV h^{-1} for 100 h (Figure 8d).

p-block metals. Currently, cationic dopants replacing Ru lattice positions have been reported in the p-block including metallic elements (Al, Ga, In, Sn, Pb, Sb, and Bi) and non-metallic elements (Te) [76-86]. Wang et al. synthesized an In-doped RuO_2 catalyst supported on graphene oxide (In-RuO_2/G) [82]. The formation of Ru−O−In local structure broke the symmetry of Ru−O−Ru in the pristine RuO_2, which significantly improved OER performance by increasing the valence state of Ru and the strength of Ru−O bonds (Figure 8e,f). Theoretical calculations confirmed that the increase in activity stemmed from the transformation of the rate-determining step from traditional *OOH formation to *OH adsorption (Figure 8g), which was attributed to the local Ru−O−In asymmetric structure weakening the barrier of *OOH formation. A recent study implemented the doping of a series of p-block elements (Ga, In, and Sn) into the lattice of RuO_2, which led to the construction of different M−O−Ru local structures that could alter Ru−O covalency [80]. Experimental characterization coupled with theoretical calculations proved that Ga-RuO_2 with moderate Ru−O covalency had the superior activity, surpassing In-RuO_2 and Sn-RuO_2 (Figure 9a). It was found that interfacial free-H_2O enriched microenvironment significantly facilitated OER kinetics of Ga-RuO_2 (Figure 9b,c). Further, Mu et al. demonstrated that p-p orbital hybridization in Al, Ga, or In doped RuO_x had a stronger stabilizing effect on lattice oxygen compared to d-p orbital hybridization in RuO_x doped with 3d elements (Mn, Co, Cu) [81]. In situ characterizations combined with DFT calculations indicated that the p-p orbital hybridization could effectively reduce the reactivity of lattice oxygen and promote the transition of the OER reaction pathway from LOM to AEM. Stabilizing lattice oxygen and inhibiting lattice oxygen participating in the reaction at high potential are crucial strategies to improve the stability of RuO_2-based catalysts. Introducing large-size and acid-resistant Pb into RuO_2 lattice can narrow the moving channel of oxygen atoms by a pinning effect, which will effectively inhibit lattice oxygen from participating in the OER process (Figure 9d) [84]. Experimental and calculations further revealed that the 6*s*-2*p*-4*d* orbital hybridization caused by Pb doping was responsible for optimizing the adsorption of reaction intermediates and reducing the covalency of Ru−O bonds, which thereby improved the OER activity and stabilized the lattice oxygen. Accordingly, the Pb-RuO_2 catalyst exhibited a low overpotential of 188 ± 2 mV to achieve a current density of 10 mA cm^{-2} and long-term durability for 1100 h with an ultralow degradation rate of only 19 μV h^{-1} (Figure 9e). Yang et al. synthesized a Bi-RuO_2 single-atom alloy oxide (SAAO) with excellent OER performance (Figure 9f-h) [77]. The introduction of single atom Bi increased the valence state of Ru and generated more oxygen vacancies (Figure 9i), which was beneficial to increase the activity of Ru sites. The experimental characterization coupled with DFT calculations proved that Bi-RuO_2 SAAO followed the AEM pathway. In addition, the incorporation of single atom Bi improved the demetallation energy of surface Ru atoms (Figure 9j), thus ensuring the structural stability of the catalyst. All in all, single-element doped RuO_2-based catalysts with modulated electronic structure demonstrated much improved activity and stability toward acidic OER.

5.1.2. Co-doping

In contrast with monodoping, the co-doping strategy can synergistically engineer the electronic structure of RuO_2 through the complementary effect of different dopants [87-100]. Therefore, there is a greater potential to break the trade-off between activity and stability of RuO_2-based catalyst by co-doping strategies.

Liu et al. synthesized a Sr and Ta co-doped RuO_2 catalyst (TS-$SrTaRuO_2$) with tensile strain [97]. The tensile strain led to elongated Ru−O bonds, which reduced the Ru−O covalency, thus suppressing the LOM mechanism, avoiding lattice oxygen participation and enhancing stability (Figure 10a). The enhancement of activity arose from the synergistic optimization of adsorption and deprotonation of active intermediates on the Ru−O active center by dual-doping of Sr and Ta, which contributed to the accelerated OER kinetics. Benefiting from the improved activity and stability, the as-prepared TS-$Sr_{0.1}Ta_{0.1}Ru_{0.8}O_{2-x}$ catalysts demonstrated an overpotential as low as 166 mV to reach 10 mA cm^{-2}, and extraordinary stability with a degradation rate of only 20 μV h^{-1} for 1000 h at 10 mA cm^{-2}. Zhou et al. reported a novel co-doping strategy of sacrificial metal Zn and electron capturer W [99]. Specifically, Zn could dissolve and release electrons at the initial stage of OER, while W with high electronegativity captured the released electrons and transferred them to the Ru sites (Figure 10b-c), thereby increasing the electron density of the Ru−O−W active centers and dramatically inhibiting the overoxidation of the Ru sites. Impressively, the resulting $Ru_3Zn_{0.85}W_{0.15}O_x$ catalyst required an overpotential of 200 mV to deliver the current density of 10 mA cm^{-2} and can be operated stably without obvious performance decay for more than 4000 h at 10 mA cm^{-2} in 0.1 M $HClO_4$.

It is acknowledged that the multielemental synergistic effect of high-entropy oxides is beneficial for the improvement of catalytic performance and stability. Hu et al. synthesized a M-$RuIrFeCoNiO_2$ with abundant grain boundaries (GBs) (Figure 10d) [91]. The multielemental synergistic effect of this quinary high-entropy oxide along with the coupling of the grain boundaries was responsible for the enhancement of the catalytic activity and stability. Consequently, the M-$RuIrFeCoNiO_2$ catalyst showed a low overpotential of 189 mV at 10 mA cm^{-2} with a high turnover frequency value of 0.24 O_2 s^{-1} at the overpotential of 300 mV, significantly outperforming commercial RuO_2 (0.02 O_2 s^{-1}) (Figure 10e,f). The assembled PEMWE using M-$RuIrFeCoNiO_2$ as the anode catalysts maintained exceptional stability during the operation over 500 h at 1 A cm^{-2} (Figure 10g). In conclusion, the multielement co-doping strategy favors optimize the electronic structure and reaction pathways of the RuO_2-based catalysts through complementary synergistic effects, thus enhancing the acidic OER performance more comprehensively.

5.2. Anion doping

Anion doping, including non-metallic elements B, S, Cl, Se, etc. has been shown to be an effective strategy to enhance the OER performance of RuO_2 [41, 101-104]. Chen et al. reported a B-doped RuO_2 with a long-range disordered structure, showing an overpotential of only 175 mV with long-term durability of 1200 h at 10 mA cm^{-2} [101]. Experiments coupled theoretical calculations demonstrated that the introduction of B atoms into RuO_2 was able to induce the formation of a long-range disorder structure and an asymmetric B−Ru−O structure, which endowed the catalyst with certain structural toughness, caused charge redistribution, and reduced Ru−O covalency (Figure 11a,b), thus improving the activity and stability of the catalyst.

Despite the LOM pathway with accelerated reaction kinetics, the involvement of lattice oxygen may lead to overoxidation and dissolution of Ru sites. Therefore, rapid replenishment of vacancies generated by lattice oxygen oxidation can improve the stability of RuO_2 catalyst for LOM. Very recently, Wu et al. reported an S-doped RuO_2 ($RuS_{0.45}O_x$) catalyst with S-substituted lattice oxygen position and SO_4^{2-}-modified surface [41]. It was found that the formed S−Ru−O structure and Ru-SO_4 localized microenvironment were responsible for the dynamic reconstruction of interfacial water from hydrogen-bonded water to free water. Consequently, a continuous free water-enriched localized microenvironment was formed on the surface of $RuS_{0.45}O_x$, which promoted the dissociation of interfacial water to achieve the replenishment of vacancies generated by lattice-oxygen oxidation (Figure 11d), thus endowing the catalyst with good structural stability. The resulting $RuS_{0.45}O_x$ showed superior activity with an ultralow potential of 160 mV at 10 mA cm^{-2} (Figure 11c), and excellent stability for 1000 h at 10 mA cm^{-2} and 500 h at 100 mA cm^{-2}.

The synthesis of RuO_2-based OER electrocatalysts usually uses $RuCl_3$ and its hydrates as precursors, which inevitably leads to the presence of chloride residues in the final catalysts. Chen et al. investigated the mechanism of the effect of residual chloride on the OER catalytic performance and reaction pathways in RuO_2-based catalysts [102]. It was found that the stability of chloride-containing RuO_2 (RuO_2-Cl) was three times higher than that of pure RuO_2 under similar conditions of morphology and crystallinity. The overpotential of RuO_2-Cl was only 176 mV at 10 mA cm^{-2}. Experimental characterization and theoretical calculations showed that the introduction of Cl not only inhibited the LOM pathway by doubly substituting bridging O atoms and decreasing Ru−O covalency (Figure 11f), but also enhanced the binding of *OOH intermediates in the AEM pathway and then reduced the reaction energy barrier (Figure 11e). As a result, the stability and catalytic activity of the RuO_2-Cl catalyst were greatly improved. Furthermore, the RuO_2-Cl catalyst in situ grown on a Pt-coated Ti felt demonstrated excellent stability for 1200 h at 100 mA cm^{-2} and 300 h at 250 mA cm^{-2}. Although anion doping has shown great potential in enhancing the OER performance and durability of RuO_2, the elemental kinds of anion dopants are quite limited compared to cation dopants.

5.3. Cation-anion dual doping

In addition to monodoping of cations or anions, cation-anion dual doping strategies with multiple roles have also been reported [43, 45, 105, 106]. Coordination-unsaturated lattice oxygen on the surface of RuO_2 is prone to overoxidation at high potentials, which in turn leads to the formation of oxygen vacancies and the dissolution of adjacent Ru sites. A novel oxyanion protection strategy was proposed, in which Ba-anchored sulfate could suppress the overoxidation of oxygen sites through the formation of coordination-saturated lattice oxygen, thereby diminishing the overoxidation of Ru (Figure 12a-c) [106]. In addition, the sulfate weakened the adsorption of the reaction intermediates, together with the role of W in promoting the formation of *OOH by accelerating the deprotonation of chemisorbed water, to enhance the OER reactivity of catalyst. The obtained $Ba_{0.3}(SO_4)_{\delta}W_{0.2}Ru_{0.5}O_{2-\delta}$ catalyst showed a low overpotential of 206 mV at 10 mA cm^{-2} with outstanding stability of 1000 h. The assembled PEMWE maintained stable operation for 300 h at 500 mA cm^{-2}. Such an oxygen anion protection strategy demonstrates excellent effectiveness in shielding the lattice oxygen from oxidation. Another strategy is to avoid the oxidative release of lattice oxygen in the vicinity of Ru sites by direct substitution of lattice oxygen, which can be combined with cation doping strategy to jointly enhance the stability of the RuO_2-based catalysts. Li et al. developed a Cr, B-codoped RuO_2 nanofibers with Ru−B−Cr active centers (Figure 12d), showing overall water-splitting performance in acidic conditions [43]. The incorporation of Cr and B dopants circumvented the occurrence of lattice oxygen oxidation and prevented the overoxidation of Ru sites, thus ensuring the stability of Ru sites. The formed Ru−B−Cr structure optimized the adsorption energy of HER and OER intermediates (Figure 12e), thus achieving bifunctional activity. As a result, the Cr, B-doped RuO_2 nanofibers required ultralow overpotentials of 205 mV and 379 mV to reach 1 A cm^{-2} and operated stably for 1000 h and 188 h at 1 A cm^{-2}, for HER and OER, respectively.

5.4. Interstitial doping

The implementation of interstitial doping requires the dopant with a small ion radius, such as H, C, Si, etc [42, 107-109]. He et al. reported the construction of Ru−O−H bond by proton and electron co-doping [107]. It was confirmed that interstitial hydrogen of Ru−O−H tended to combine with adjacent oxygen to form a hydrogen bond (Ru−O−H…O) that favored enhanced activity and lattice oxygen stability. Acid-resistant Si with a small ionic radius could be inserted into the interstitial sites of RuO_2 and form strong Si−O bonds, which prevented lattice oxygen oxidation and weakened the Ru−O covalency, thus inhibiting the LOM pathway and stabilizing the Ru sites (Figure 13a) [42]. Since the induction of Si lowered the energy barrier for *OOH formation, thereby enhancing the OER activity. Thus, the resulting Si-RuO_2-0.1 catalyst demonstrated a low overpotential of 226 mV and high stability for 800 h at 10 mA cm^{-2} with a low degradation rate of 52 μV h^{-1}. In addition, the introduction of interstitial C has been proven to be effective in enhancing the performance of RuO_2 catalysts [109]. The C−O bond formed by the introduction of interstitial C elongated the Ru−O bond, leading to a decrease in the OER energy barrier and an increase in the dissociation energy of lattice oxygen (Figure 13b,c), thus enhancing the activity and stability of RuO_2-based catalyst (Figure 13d). In conclusion, interstitial doping still needs to be further developed, and the change of dopants in OER process needs to be studied in depth.

5.5. Solid solution oxides

RuO_2-based bimetallic/polymetallic solid solution oxides can be generated by incorporating foreign metal elements into the RuO_2 matrix [113, 117-123]. The formation of solid solutions requires similar ionic radii, close electronegativities, and the same crystal structure between the solute and the solvent [44, 110-112, 114, 115]. Cr is an attractive candidate for forming solid solution oxides with Ru. For instance, Lin et al. synthesized a Cr−Ru solid solution oxide based on a metal-organic framework template i.e., MIL-101 (Cr), and the resulting rutile $Cr_{0.6}Ru_{0.4}O_2$ electrocatalyst showed a low overpotential of 178 mV at 10 mA cm^{-2} [112]. DFT calculations revealed that the improvement of OER activity and stability originated from the modulation of the electronic structure of RuO_2 phase by Cr promoter. In this study, the OER reaction pathway followed the AEM mechanism. Another study by Cao et al. found that Cr in $Cr_xRu_{1-x}O_2$ solid solution could accelerate water dissociation and function as a Lewis acid site to enhance OH adsorption, thus boosting the generation of *O radical [111]. Due to the introduction of Cr with smaller lattice parameters, the interatomic distance between Ru−Cr dual sites in $Cr_xRu_{1-x}O_2$ solid solutions was shortened compared to RuO_2, thereby promoting O−O radical coupling (Figure 14a-c). Benefiting from the OPM pathway, the resulting $Cr_{0.6}Ru_{0.4}O_2$ electrocatalyst demonstrated a low overpotential of 220 mV at 10 mA cm^{-2} and superior stability for 300 h at 50 mA cm^{-2}, as well as exceptional long-term durability for 350 h at 300 mA cm^{-2} in a PEMWE. The distinct OER pathway followed by two Cr−Ru solid solution oxide electrocatalysts was attributed to the difference of calculation parameters and simulation models.

Due to the presence of complex PCET steps for OER, the influence of proton transfer rate on OER kinetics is obvious. Wen et al. introduced the strong Brønsted acid site WO_x into RuO_2 to prepare a Ru-W binary solid solution oxide electrocatalyst [122]. The formed W-O_{bri}-Ru bridging oxygen sites increased proton mobility, resulting in a rapid bridging oxygen-assisted deprotonation process for OER intermediates. Due to the acceleration of OER kinetics, the $Ru_5W_1O_x$ catalyst exhibits a low overpotential of 235 mV at 10 mA cm^{-2} and exceptional long-term stability over 550 h with a low degradation of 14 μV h^{-1}. Notably, the universality of this strategy has also been confirmed in other Ru−M (M = Ti, Cr, Nb, Mo, and Ta) binary metal oxides. Similarly, Hu et al. also found that the incorporation of Ti can optimize the adsorption energy of protons on O_{bri} sites of $RuTiO_x$ solid solution and accelerate the deprotonation of oxygen intermediates [121]. A combination of Ru and Ir can also form a solid solution oxide. Zhu et al. reported that the addition of Ir led to the generation of more Ru active sites with high oxidation states in the $Ru_{0.5}Ir_{0.5}O_2$ solid solution at low voltage [114]. The formation of the Ru−O−Ir local structure prevents overoxidation of the Ru active site, which is responsible for the stability of the $Ru_{0.5}$Ir0.$_5O_2$ solid solution. In contrast with commercial RuO_2 and IrO_2, the $Ru_{0.5}Ir_{0.5}O_2$ demonstrated much improved activity with an ultralow overpotential of 151 mV at 10 mA cm^{-2} and outstanding stability for 618.3 h.

The Ru charge can be used as the scale of the catalytic pathway, so it is feasible to customize the reaction pathway of the RuO_2-based catalyst by manipulating the Ru charge [110]. The $MRuO_x$ (M = Ce^{4+}, Sn^{4+}, Ru^{4+}, Cr^{4+}) solid solution was as the model catalyst. The OER pathways and intermediate binding energy of the catalyst were customized by manipulating the Ru charge, and subsequently the stability could be determined. The $SnRuO_x$ solid solution catalyst with moderate Ru charge, was customized to follow AEM pathway and possess moderate intermediate binding energy, which may mean high stability and activity (Figure 14d). The experimental results showed that the $SnRuO_x$ catalyst had a low overpotential of 194 mV and a slow increase of overpotential by 26.8 mV for 250 h stability test. The assembled PEMWE required only 1.565, 1.655, and 1.735 V to deliver current densities of 1, 2, and 3 A cm^{-2} (Figure 14e), respectively, and operated stably at 1 A cm^{-2} for 1300 h with the degradation rate of only 53 $\mu V\ h^{-1}$ (Figure 14f). In addition to changing the dopant elements, it is also important to study the effect of different doping amounts of the specific dopant on the reaction mechanism and performance of catalysts. Jun et al. studied the relationship between the doping amount of Mn in the $Mn_xRu_{1-x}O_2$ solid solution oxide and the OER mechanism [44]. An appropriate amount of Mn doping could lead to the increase of the oxidation state of Ru and strengthens the Ru−O bond, thereby improving the activity and stability of catalyst. Excessive Mn doping could cause a transition of OER pathway from AEM to LOM, followed by the formation of abundant oxygen vacancies and Ru dissolution.

Therefore, the $Mn_{0.2}Ru_{0.8}O_2$ catalyst with the optimal Mn doping amount showed good catalytic activity and optimal stability compared to other $Mn_xRu_{1-x}O_2$ (x=0.1, 0.3, 0.4).

The bidirectional regulation of electronic structure of Ru sites can be achieved by multimetal co-doping. Liu et al. proposed an "elastic electron transfer" strategy to modulate the electronic structure of Ru bidirectionally by electron-withdrawing Sr and Cr electron buffer [120]. The function of Sr is to absorb the electrons to increase the oxidation state of Ru, while Cr accepts the excess electrons after Sr leaching, and donates electrons to inhibit the overoxidation of Ru during OER process. The bidirectional manipulation of the electronic structure grants the catalyst high activity and stability. The resulting $Ru_3Cr_1Sr_{0.175}$ solid solution oxide electrocatalyst displayed a low overpotential of 214 mV at 10 mA cm^{-2} and superior durability over 300 h.

In addition, metal atoms with smaller atomic sizes such as Li can be inserted into lattice gaps rather than replacing Ru atoms to form a solid solution phase [116]. As an electron donor, Li intercalation decreased the valence state of Ru, thus inhibiting Ru dissolution. The formed stable Li−O−Ru local structure suppressed the lattice oxygen participation and further improved the stability of RuO_2. In addition, the dangling O atoms near the Ru site were activated owing to the surface structure distortion caused by lattice strain. These dangling O atoms as proton acceptors could stabilize *OOH, thus significantly improving OER activity of RuO_2. The resulting $Li_{0.52}RuO_2$ solid solution oxide showed an ultralow overpotential of 156 mV at 10 mA cm^{-2}.

6. Summary and outlook

In summary, doping, as a flexible, simple and practical strategy, plays an important role in modulating the electronic structure, increasing actives sites, optimizing intermediate adsorption, stabilizing lattice oxygen, and inhibiting Ru dissolution. Thus, the doping strategy shows great potential to break the bottleneck of activity and stability of RuO_2-based electrocatalysts. Accompanied by boosted reports in recent years, the catalytic performance and stability of heteroatom-doped RuO_2 have been continuously elevated. Despite the large breakthrough, there is still a big gap between experimental exploration and industrial application. The following are the current challenges and the proposed outlook.

6.1. Design of catalysts

1) Due to the scarcity and high price of Ru, the design of catalysts needs to be oriented toward the cost-effective direction by minimizing the content of Ru as much as possible. For example, reducing the particle size of RuO_2-based catalysts and improving the utilization of active sites.

2) Due to the limitation of interstitial doping on the size of dopant atoms, only very few reports have realized interstitial doping such as H, Li, C, Si. Substitutional doping especially cation doping has higher flexibility and lesser limitations for applications due to wide range of doping elements. Numerous reports on cation-doped RuO_2 have demonstrated exceptional activity and stability. For future catalyst design, on the one hand, interstitial doping strategies require the application of more new elements. On the other hand, the integration of different doping strategies, such as interstitial doping (Li, Na, C, Si) and cation doping (transition metals), may produce synergistic effects to optimize the activity and stability of RuO_2.

3) The synergistic combination of doping strategies with other strategies needs to be explored. For example, strong catalyst-support interactions, which can effectively prevent catalyst aggregation, optimize the adsorption of intermediates, and inhibit the overoxidation of Ru sites by electrons transferred from the support to RuO_2 during OER.

4) Construction of core-shell structure such as a heteroatom-doped Ru@RuO_2 core-shell heterostructure is conducive to the realization of bifunctional catalytic activity toward HER and OER. The use of bifunctional catalysts can simplify the structure of the electrolyzer, reduce the manufacturing cost of the electrolyzer, avoid cross-contamination from the leaching of two cathode-anode catalysts with different compositions.

5) Anion doping can directly substitute the position of lattice oxygen, thus avoiding Ru dissolution caused by lattice oxygen oxidation. Therefore, there is a need to develop more anion dopants such as P, F, etc. In addition, anchoring acid radical ions on the surface can stabilize lattice oxygen, which should be further developed. The roles of different acid radical ions need to be compared.

6) Due to the synergistic and complementary nature of the multielement dopants, it has a

significant advantage in dynamically regulating the electronic structure of Ru, and it can be further developed to realize high activity and stability at high potentials.

7) A combination of machine learning (ML) and density function theory (DFT) calculations was used to predict the optimal dopants, which helped to rapidly screen high-performance RuO_2-based OER catalysts.

6.2. Evaluation of catalysts

1) Currently, the elemental range of dopants is getting wider and wider, covering almost 45% of the entire periodic table. Even for the same dopant, the performance, stability, and even the reaction pathways are varied in different literatures. Hence, a simple comparison of the overpotentials and stability test time of RuO_2 with different dopants is totally insufficient. It is necessary to establish a unified standard protocol to scientifically and accurately evaluate the effectiveness of dopants based on comprehensive consideration of the doping content, preparation methods, test conditions, etc. After that, the dopants that are really effective and promising for industrialization can be screened for further development.

(2) Current stability tests usually are conducted on a small electrode with a low current density (10 mA cm^{-2}) by chronopotentiometry. In the future, it will be necessary to continuously increase the electrode size and current density to approach industrial standards.

(3) By employing various *operando* characterizations and isotope labeling techniques, it is possible to identify the true active site, monitor the structural evolution of the active species and dopants, and the dynamic changes of the intermediates, which is important for confirming reaction pathways and understanding the structure-activity-stability relationship.

6.3. Industrial applications

Currently, laboratory-grade catalysts are prepared with less consideration for cost and scalability of the method. Therefore, the first step in moving from the laboratory to industrial applications is to develop technological methods for the large-scale preparation of highly active RuO_2-based catalysts with low Ru content. Furthermore, existing industrial-grade PEMWEs require a continuous operating lifetime of 40,000 hours (~4.5 years) with a degradation rate of less than 4.8 mV kh^{-1} [126]. Thus, the stability evaluation of catalysts needs to be carried out under more demanding conditions. On one hand, the ability to adapt to high-temperature and high-pressure environments and stress resistance of the catalyst need to be verified. On the other hand, the catalyst must be evaluated for stability under real operational conditions including an accelerated aging test with step changes in current density and an intermittent stability test with start-shutdown cycles.

Acknowledgments

This work was supported by funds provided by the National Natural Science Foundation of China (22201294), Guangdong Basic and Applied Basic Research Foundation (2023A1515012370), Guangdong Pearl River Talent Program (2023QN10C361), High-level Talents Program of the CAS (E344021001), Joint Scientific Research Project Funding by the National Natural Science Foundation of China and the Macao Science and Technology Development Fund (0090/2022/AFJ), Shanghai Pujiang Program (No.23PJD002), Clean Energy Joint International Laboratory (E3G1041001), Shenzhen Science and Technology Program (KQTD20221101093647058), and SIAT Innovation Fund for Excellent Young Scientists (E3G0071001).

Disclosure statement

No potential conflict of interest was reported by the authors.

Author contributions

X.Y. designed the framework of this review article. Y.Z. wrote the manuscript. T.Z., Q.Z., H.G. and J.Y. read and modified the conclusions of manuscript. X.Y., H.S., and B.D. coedited the manuscript and approved the final version of the manuscript.

References

[1] Quan L, Jiang H, Mei G, et al. Bifunctional electrocatalysts for overall and hybrid water splitting. Chem Rev. 2024;124(7):3694-3812. DOI:10.1021/acs.chemrev.3c00332

[2] Chatenet M, Pollet B G, Dekel D R, et al. Water electrolysis: from textbook knowledge to the latest scientific strategies and industrial developments. Chem Soc Rev. 2022;51(11):4583-4762. DOI:10.1039/d0cs01079k

[3] Peng Z, Zhang Q, Qi G, et al. Nanostructured Pt@RuO_x catalyst for boosting overall acidic seawater splitting. Chin J Struct Chem. 2024;43(1):100191. DOI:10.1016/j.cjsc.2023.100191

[4] Yang X, Nielsen C P, Song S, et al. Breaking the hard-to-abate bottleneck in China’s path to carbon neutrality with clean hydrogen. Nat Energy. 2022;7(10):955-965. DOI:10.1038/s41560-022-01114-6

[5] Luo Y, Zhang S, Pan H, et al. Unsaturated single atoms on monolayer transition metal dichalcogenides for ultrafast hydrogen evolution. ACS Nano. 2019;14(1):767-776. DOI:10.1021/acsnano.9b07763

[6] Yu Z Y, Duan Y, Feng X Y, et al. Clean and affordable hydrogen fuel from alkaline water splitting: past, recent progress, and future prospects. Adv Mater. 2021;33(31):2007100. DOI:10.1002/adma.202007100

[7] Chu S, Majumdar A. Opportunities and challenges for a sustainable energy future. Nature. 2012;488(7411):294-303. DOI:10.1038/nature11475

[8] Yu Q, Zhang Z, Qiu S, et al. A Ta-TaS_2 monolith catalyst with robust and metallic interface for superior hydrogen evolution. Nat Commun. 2021;12:6051. DOI:10.1038/s41467-021-26315-7

[9] Henkensmeier D, Cho W-C, Jannasch P, et al. Separators and membranes for advanced alkaline water electrolysis. Chem Rev. 2024;124(10):6393-6443. DOI:10.1021/acs.chemrev.3c00694

[10] Wang C R, Stansberry J M, Mukundan R, et al. Proton exchange membrane (PEM) water electrolysis: cell-level considerations for gigawatt-scale deployment. Chem Rev. 2025;125(3):1257-1302. DOI:10.1021/acs.chemrev.3c00904

[11] Chen F-Y, Wu Z-Y, Adler Z, et al. Stability challenges of electrocatalytic oxygen evolution reaction: from mechanistic understanding to reactor design. Joule. 2021;5(7):1704-1731. DOI:10.1016/j.joule.2021.05.005

[12] Hu H, Liu S, Sun H, et al. Low-Ir-content $Ir_{0.10}Mn_{0.90}O_2$ solid solution for highly active oxygen evolution in acid media. Small. 2025;2412096. DOI:10.1002/smll.202412096

[13] Yu F, Zhou H, Huang Y, et al. High-performance bifunctional porous non-noble metal phosphide catalyst for overall water splitting. Nat Commun. 2018;9:2551. DOI:10.1038/s41467-018-04746-z

[14] Qin L, Zhang W, Cao R. Hydrophilic MnO_2 nanowires coating with o-fluoroaniline for electrocatalytic water oxidation. Chin J Struct Chem. 2023;42(8):100105. DOI:10.1016/j.cjsc.2023.100105

[15] Shi Q, Zhu C, Du D, et al. Robust noble metal-based electrocatalysts for oxygen evolution reaction. Chem Soc Rev. 2019;48(12):3181-3192. DOI:10.1039/c8cs00671g

[16] Seh Z W, Kibsgaard J, Dickens C F, et al. Combining theory and experiment in electrocatalysis: insights into materials design. Science. 2017;355(6321):eaad4998 DOI:10.1126/science.aad4998

[17] Li S, Chen B, Wang Y, et al. Oxygen-evolving catalytic atoms on metal carbides. Nat Mater. 2021;20(9):1240-1247. DOI:10.1038/s41563-021-01006-2

[18] Hao S, Sheng H, Liu M, et al. Torsion strained iridium oxide for efficient acidic water oxidation in proton exchange membrane electrolyzers. Nat Nanotechnol. 2021;16(12):1371-1377. DOI:10.1038/s41565-021-00986-1

[19] Seitz L C, Dickens C F, Nishio K, et al. A highly active and stable $IrO_x/SrIrO_3$ catalyst for the oxygen evolution reaction. Science. 2016;353(6303):1011-1014. DOI:10.1126/science.aaf5050

[20] Wang Y, Zhang M, Kang Z, et al. Nano-metal diborides-supported anode catalyst with strongly coupled TaO_x/IrO_2 catalytic layer for low-iridium-loading proton exchange membrane electrolyzer. Nat Commun. 2023;14:5119. DOI:10.1038/s41467-023-40912-8

[21] Gao J, Xu C-Q, Hung S-F, et al. Breaking long-range order in iridium oxide by alkali ion for efficient water oxidation. J Am Chem Soc. 2019;141(7):3014-3023. DOI:10.1021/jacs.8b11456

[22] Rao R R, Kolb M J, Giordano L, et al. Operando identification of site-dependent water oxidation activity on ruthenium dioxide single-crystal surfaces. Nat Catal. 2020;3(6):516-525. DOI:10.1038/s41929-020-0457-6

[23] Yao Y, Hu S, Chen W, et al. Engineering the electronic structure of single atom Ru sites via compressive strain boosts acidic water oxidation electrocatalysis. Nat Catal. 2019;2(4):304-313. DOI:10.1038/s41929-019-0246-2

[24] Li L, Wang P, Shao Q, et al. Recent progress in advanced electrocatalyst design for acidic oxygen evolution reaction. Adv Mater. 2021;33(50):2004243. DOI:10.1002/adma.202004243

[25] An L, Wei C, Lu M, et al. Recent development of oxygen evolution electrocatalysts in acidic environment. Adv Mater. 2021;33(20):2006328. DOI:10.1002/adma.202006328

[26] Spöri C, Kwan J T H, Bonakdarpour A, et al. The stability challenges of oxygen evolving catalysts: towards a common fundamental understanding and mitigation of catalyst degradation. Angew Chem Int Ed. 2017;56(22):5994-6021. DOI:10.1002/anie.201608601

[27] Niu Z, Lu Z, Qiao Z, et al. Robust Ru-VO_2 bifunctional catalysts for all-pH overall water splitting. Adv Mater. 2023;36(9):2310690. DOI:10.1002/adma.202310690

[28] Pei Z, Zhang H, Luan D, et al. Electrocatalytic acidic oxygen evolution: from catalyst design to industrial applications. Matter. 2023;6(12):4128-4144. DOI:10.1016/j.matt.2023.11.007

[29] Rong C, Dastafkan K, Wang Y, et al. Breaking the activity and stability bottlenecks of electrocatalysts for oxygen evolution reactions in acids. Adv Mater. 2023;35(49):2211884. DOI:10.1002/adma.202211884

[30] Qin R, Chen G, Feng X, et al. Ru/Ir-based electrocatalysts for oxygen evolution reaction in acidic conditions: from mechanisms, optimizations to challenges. Advanced Science. 2024;11(21):2309364. DOI:10.1002/advs.202309364

[31] Fan R Y, Zhang Y S, Lv J Y, et al. The promising seesaw relationship between activity and stability of Ru-based electrocatalysts for acid oxygen evolution and proton exchange membrane water electrolysis. Small. 2023;20(5):2304636. DOI:10.1002/smll.202304636

[32] Lin Y, Dong Y, Wang X, et al. Electrocatalysts for the oxygen evolution reaction in acidic media. Adv Mater. 2023;35(22):2210565. DOI:10.1002/adma.202210565

[33] Chen D, Yu R, Yu K, et al. Bicontinuous RuO_2 nanoreactors for acidic water oxidation. Nat Commun. 2024;15:3928. DOI:10.1038/s41467-024-48372-4

[34] Shan J, Zheng Y, Shi B, et al. Regulating electrocatalysts via surface and interface engineering for acidic water electrooxidation. ACS Energy Lett. 2019;4(11):2719-2730. DOI:10.1021/acsenergylett.9b01758

[35] Liu Y, Liang X, Chen H, et al. Iridium-containing water-oxidation catalysts in acidic electrolyte. Chinese J Catal. 2021;42(7):1054-1077. DOI:10.1016/s1872-2067(20)63722-6

[36] Wang Q, Cheng Y, Tao H B, et al. Long-term stability challenges and opportunities in acidic oxygen evolution electrocatalysis. Angew Chem Int Ed. 2023;62(11):e202216645. DOI:10.1002/anie.202216645

[37] Chang J, Shi Y, Wu H, et al. Oxygen radical coupling on short-range ordered Ru atom arrays enables exceptional activity and stability for acidic water oxidation. J Am Chem Soc. 2024;146(19):12958-12968. DOI:10.1021/jacs.3c13248

[38] Lin C, Li J-L, Li X, et al. In-situ reconstructed Ru atom array on α-MnO_2 with enhanced performance for acidic water oxidation. Nat Catal. 2021;4(12):1012-1023. DOI:10.1038/s41929-021-00703-0

[39] Zhu W, Yao F, Cheng K, et al. Direct dioxygen radical coupling driven by octahedral ruthenium–oxygen–cobalt collaborative coordination for acidic oxygen evolution reaction. J Am Chem Soc. 2023;145(32):17995-18006. DOI:10.1021/jacs.3c05556

[40] Su J, Ge R, Jiang K, et al. Assembling ultrasmall copper-doped ruthenium oxide nanocrystals into hollow porous polyhedra: highly robust electrocatalysts for oxygen evolution in acidic media. Adv Mater. 2018;30(29):1801351. DOI:10.1002/adma.201801351

[41] Wu L, Huang W, Li D, et al. Role of interfacial water in improving the activity and stability of lattice-oxygen-mediated acidic oxygen evolution on RuO_2. Angew Chem Int Ed. 2025;e202420848 DOI:10.1002/anie.202420848

[42] Ping X, Liu Y, Zheng L, et al. Locking the lattice oxygen in RuO_2 to stabilize highly active Ru sites in acidic water oxidation. Nat Commun. 2024;15:2501. DOI:10.1038/s41467-024-46815-6

[43] Li W, Zhang L, Ma L, et al. Designing Ru–B–Cr moieties to activate the Ru site for acidic water electrolysis under industrial-level current density. Nano Lett. 2024;25(1):443-452.

DOI:10.1021/acs.nanolett.4c05113

[44] Jun H, Kang E, Moon J, et al. Quantity effect of heteroatom incorporation on the oxygen evolution mechanism in ruthenium oxide. Chem. 2024;102367. DOI:10.1016/j.chempr.2024.11.005

[45] Xue Y, Fang J, Wang X, et al. Sulfate-functionalized $RuFeO_x$ as highly efficient oxygen evolution reaction electrocatalyst in acid. Adv Funct Mater. 2021;31(32):2101405. DOI:10.1002/adfm.202101405

[46] Li Z, Wang S, Tian Y, et al. Mg-doping improves the performance of Ru-based electrocatalysts for the acidic oxygen evolution reaction. Chem Commun. 2020;56(11):1749-1752. DOI:10.1039/c9cc09613b

[47] Zhang L, Jang H, Liu H, et al. Sodium-decorated amorphous/crystalline RuO_2 with rich oxygen vacancies: a robust pH-universal oxygen evolution electrocatalyst. Angew Chem Int Ed. 2021;60(34):18821-18829. DOI:10.1002/anie.202106631

[48] Yang Y, Guo J, Xu L, et al. Bond engineering: weakening Ru–O covalency for efficient and stable water oxidation in acidic solutions. J Energy Chem. 2025;102:1-9. DOI:10.1016/j.jechem.2024.09.070

[49] Li W, Chen D, Lou Z, et al. Inhibiting overoxidation of dynamically evolved RuO_2 to achieve a win–win in activity–stability for acidic water electrolysis. J Am Chem Soc. 2025;147(12):10446-10458. DOI:10.1021/jacs.4c18300

[50] Wang Y, Yang R, Ding Y, et al. Unraveling oxygen vacancy site mechanism of Rh-doped RuO_2 catalyst for long-lasting acidic water oxidation. Nat Commun. 2023;14:1412. DOI:10.1038/s41467-023-37008-8

[51] Wu H, Chang J, Yu J, et al. Atomically engineered interfaces inducing bridging oxygen-mediated deprotonation for enhanced oxygen evolution in acidic conditions. Nat Commun. 2024;15:10315. DOI:10.1038/s41467-024-54798-7

[52] Park Y, Jang H Y, Lee T K, et al. Atomic-level Ru-Ir mixing in rutile-type $(RuIr)O_2$ for efficient and durable oxygen evolution catalysis. Nat Commun. 2025;16:579. DOI:10.1038/s41467-025-55910-1

[53] Li X, Chen G, Liu Y, et al. Optimal selection of RuO_2 for durable oxygen evolution reactions in acidic media by continuous regulation of Ru–O covalency. Energy Environ Sci. 2025; DOI:10.1039/d4ee04861j

[54] Shen Y, Zhang X-L, Qu M-R, et al. Cr dopant mediates hydroxyl spillover on RuO_2 for high-efficiency proton exchange membrane electrolysis. Nat Commun. 2024;15:7861. DOI:10.1038/s41467-024-51871-z

[55] Chen S, Huang H, Jiang P, et al. Mn-doped RuO_2 nanocrystals as highly active electrocatalysts for enhanced oxygen evolution in acidic media. ACS Catal. 2019;10(2):1152-1160. DOI:10.1021/acscatal.9b04922

[56] Zhao S, Dang Q, Cao A, et al. Hydroxylation strategy enables Ru–Mn oxide for stable proton exchange membrane water electrolysis under 1 A cm^{-2}. ACS Nano. 2025;19(9):8773-8785. DOI:10.1021/acsnano.4c15900

[57] Zhang Y, Dong J, Sun T, et al. Mo-doped mesoporous RuO_2 spheres as high-performance acidic oxygen evolution reaction electrocatalyst. Small. 2023;20(11):2305889. DOI:10.1002/smll.202305889

[58] Liu H, Zhang Z, Fang J, et al. Eliminating over-oxidation of ruthenium oxides by niobium for highly stable electrocatalytic oxygen evolution in acidic media. Joule. 2023;7(3):558-573. DOI:10.1016/j.joule.2023.02.012

[59] Wu Z-Y, Chen F-Y, Li B, et al. Non-iridium-based electrocatalyst for durable acidic oxygen evolution reaction in proton exchange membrane water electrolysis. Nat Mater. 2022;22(1):100-108. DOI:10.1038/s41563-022-01380-5

[60] Jin H, Liu X, An P, et al. Dynamic rhenium dopant boosts ruthenium oxide for durable oxygen evolution. Nat Commun. 2023;14:354. DOI:10.1038/s41467-023-35913-6

[61] Wang X, Li Z, Jang H, et al. RuO_2 with short-range ordered tantalum single atoms for enhanced acidic oxygen evolution reaction. Adv Energy Mater. 2024;15(6):2403388. DOI:10.1002/aenm.202403388

[62] Zhang J, Fu X, Kwon S, et al. Tantalum-stabilized ruthenium oxide electrocatalysts for industrial water electrolysis. Science. 2025;387(6729):48–55 DOI:10.1126/science.ado9938

[63] Qin Q, Li Z, Zhao X, et al. Atomically dispersed vanadium-induced Ru-V dual active sites enable exceptional performance for acidic water oxidation. Angew Chem Int Ed. 2024;64(1):e202413657. DOI:10.1002/anie.202413657

[64] Sun P, Qiao Z, Dong X, et al. Designing 3d transition metal cation-doped $MRuO_x$ as durable acidic oxygen evolution electrocatalysts for PEM water electrolyzers. J Am Chem Soc. 2024;146(22):15515-15524. DOI:10.1021/jacs.4c04096

[65] Zhang D, Li M, Yong X, et al. Construction of Zn-doped RuO_2 nanowires for efficient and stable water oxidation in acidic media. Nat Commun. 2023;14:2517. DOI:10.1038/s41467-023-38213-1

[66] Liu M, Chen X, Li S, et al. Dynamic-cycling zinc sites promote ruthenium oxide for sub-ampere electrochemical water oxidation. Nano Lett. 2024;24(50):16055-16063. DOI:10.1021/acs.nanolett.4c04485

[67] Zhang H, Wu B, Su J, et al. MOF-derived zinc-doped ruthenium oxide hollow nanorods as highly active and stable electrocatalysts for oxygen evolution in acidic media. ChemNanoMat. 2021;7(2):117-121. DOI:10.1002/cnma.202000526

[68] Zhai T, Gao X, Wang H, et al. Ultrafine semi-crystalline Y-doped RuO_2 for highly active and durable proton-exchange-membrane water electrolysis. Matter. 2025;8(5):102141. DOI:10.1016/j.matt.2025.102141

[69] Boakye F O, Harrath K, Zhang D, et al. Synergistic engineering of dopant and support of Ru oxide catalyst enables ultrahigh performance for acidic oxygen evolution. Adv Funct Mater. 2024;34(48):2408714. DOI:10.1002/adfm.202408714

[70] Wu L, Yao N, Meng Q, et al. Manipulating reaction pathway of ruthenium oxide with enhanced performance and stability toward acidic water oxidation. Chem Catal. 2024;4(6):101004. DOI:10.1016/j.checat.2024.101004

[71] Li L, Zhang G, Zhou C, et al. Lanthanide-regulating Ru-O covalency optimizes acidic oxygen evolution electrocatalysis. Nat Commun. 2024;15:4974. DOI:10.1038/s41467-024-49281-2

[72] Zhang X Y, Yin H, Dang C C, et al. Unlocking enhanced catalysis stability in acidic

oxygen evolution: structural insights for PEM applications under high-current density. Angew Chem Int Ed. 2025;e202425569. DOI:10.1002/anie.202425569

[73] Wu Y, Yao R, Zhao Q, et al. La-RuO_2 nanocrystals with efficient electrocatalytic activity for overall water splitting in acidic media: Synergistic effect of La doping and oxygen vacancy. Chem Eng J. 2022;439:135699. DOI:10.1016/j.cej.2022.135699

[74] Li L, Zhang G, Xu J, et al. Optimizing the electronic structure of ruthenium oxide by neodymium doping for enhanced acidic oxygen evolution catalysis. Adv Funct Mater. 2023;33(10):2213304. DOI:10.1002/adfm.202213304

[75] Wang C, Wu X, Sun H, et al. An asymmetric RE–O–Ru unit with bridged oxygen vacancies accelerates deprotonation during acidic water oxidation. Energy Environ Sci. 2025;18(9):4276-4287. DOI:10.1039/d5ee00281h

[76] Niu Z, Qiao Z, Sun P, et al. Single-atom Sb-doped $RuSbO_x$ bifunctional catalysts for ultra-stable PEM water electrolyzers. Small. 2025;2502088. DOI:10.1002/smll.202502088

[77] Yang Z, Ding Y, Chen W, et al. Phase-engineered Bi-RuO_2 single-atom alloy oxide boosting oxygen evolution electrocatalysis in proton exchange membrane water electrolyzer. Adv Mater. 2025;37(9):2417777. DOI:10.1002/adma.202417777

[78] Wu L, Liang Q, Zhao J, et al. A Bi-doped RuO_2 catalyst for efficient and durable acidic water oxidation. Chinese J Catal. 2023;55:182-190. DOI:10.1016/s1872-2067(23)64554-1

[79] Lee K, Shim J, Jang H Y, et al. Modulating the valence electronic structure using earth-abundant aluminum for high-performance acidic oxygen evolution reaction. Chem. 2023;9(12):3600-3612. DOI:10.1016/j.chempr.2023.08.006

[80] Wu L, Huang W, Li D, et al. Unveiling the structure and dissociation of interfacial water on RuO_2 for efficient acidic oxygen evolution reaction. Angew Chem Int Ed. 2024;64(1):e202413334. DOI:10.1002/anie.202413334

[81] Mu Y, Zhang D, Gao T, et al. p–p orbital hybridization stabilizing lattice oxygen in two-dimensional amorphous RuO_x for efficient acidic oxygen evolution. Angew Chem Int Ed. 2025;e202505908. DOI:10.1002/anie.202505908

[82] Wang Y, Lei X, Zhang B, et al. Breaking the Ru−O−Ru symmetry of a RuO_2 catalyst for sustainable acidic water oxidation. Angew Chem Int Ed. 2023;63(3):e202316903. DOI:10.1002/anie.202316903

[83] Chen F-Y, Qiu C, Wu Z-Y, et al. Ruthenium-lead oxide for acidic oxygen evolution reaction in proton exchange membrane water electrolysis. Nano Res. 2024;17(10):8671-8677. DOI:10.1007/s12274-024-6460-5

[84] Zhou C, Li L, Dong Z, et al. Pinning effect of lattice Pb suppressing lattice oxygen reactivity of Pb-RuO_2 enables stable industrial-level electrolysis. Nat Commun. 2024;15:9774. DOI:10.1038/s41467-024-53905-y

[85] Qiu L, Zheng G, He Y, et al. Ultra-small Sn-RuO_2 nanoparticles supported on N-doped carbon polyhedra for highly active and durable oxygen evolution reaction in acidic media. Chem Eng J. 2021;409:128155. DOI:10.1016/j.cej.2020.128155

[86] Liu G Q, Yang Y, Zhang X L, et al. Porous tellurium-doped ruthenium dioxide nanotubes for enhanced acidic water oxidation. Small. 2023;20(16):2306914. DOI:10.1002/smll.202306914

[87] Zhou Y-N, Fan R-Y, Zhang Y-S, et al. Self-catalyzed Ru redeposition based on Co, Zn-driven double anchoring for robust acidic water oxidation. ACS Energy Lett. 2024;9(10):5064-5073. DOI:10.1021/acsenergylett.4c02475

[88] Abed J, Heras-Domingo J, Sanspeur R Y, et al. Pourbaix machine learning framework identifies acidic water oxidation catalysts exhibiting suppressed ruthenium dissolution. J Am Chem Soc. 2024;146(23):15740-15750. DOI:10.1021/jacs.4c01353

[89] Sun Y, Xiao M, Liu F, et al. Oxygen vacancy-electron polarons featured $InSnRuO_2$ oxides: orderly and concerted In-Ov-Ru-O-Sn substructures for acidic water oxidation. Adv Mater. 2024;36(52):2414579. DOI:10.1002/adma.202414579

[90] Miao X, Peng Z, Shi L, et al. Insulating high-entropy ruthenium oxide as a highly efficient oxygen-evolving electrocatalyst in acid. ACS Catal. 2023;13(6):3983-3989. DOI:10.1021/acscatal.2c06276

[91] Hu C, Yue K, Han J, et al. Misoriented high-entropy iridium ruthenium oxide for acidic

water splitting. Sci Adv. 2023;9(37):eadf9144. DOI:10.1126/sciadv.adf9144

[92] Zhang T, Liu Q, Bao H, et al. Atomically thin high-entropy oxides via naked metal ion self-assembly for proton exchange membrane electrolysis. Nat Commun. 2025;16:1037. DOI:10.1038/s41467-025-56189-y

[93] Lun Y, Chen H, Wang K, et al. Discovery of efficient acidic oxygen evolution electrocatalyst: high-throughput computational screening of MgIrRu oxide. Adv Energy Mater. 2025;2405657. DOI:10.1002/aenm.202405657

[94] Zhu Y, Wu F, Zhang X, et al. Engineering lattice distortion in ruthenium oxide enables robust acidic water oxidation via direct O–O coupling. Adv Mater. 2025;2500449. DOI:10.1002/adma.202500449

[95] Jin H, Choi S, Bang G J, et al. Safeguarding the RuO_2 phase against lattice oxygen oxidation during acidic water electrooxidation. Energy Environ Sci. 2022;15(3):1119-1130. DOI:10.1039/d1ee02636d

[96] Wen Y, Chen P, Wang L, et al. Stabilizing highly active Ru sites by suppressing lattice oxygen participation in acidic water oxidation. J Am Chem Soc. 2021;143(17):6482-6490. DOI:10.1021/jacs.1c00384

[97] Liu Y, Wang Y, Li H, et al. Effectiveness of strain and dopants on breaking the activity-stability trade-off of RuO_2 acidic oxygen evolution electrocatalysts. Nat Commun. 2025;16:1717. DOI:10.1038/s41467-025-56638-8

[98] Hao S, Liu M, Pan J, et al. Dopants fixation of ruthenium for boosting acidic oxygen evolution stability and activity. Nat Commun. 2020;11:5368. DOI:10.1038/s41467-020-19212-y

[99] Zhou K, Liu H, Liu Z, et al. W-mediated electron accumulation in Ru−O−W motifs enables ultra-stable oxygen evolution reaction in acid. Angew Chem Int Ed. 2025;e202422707. DOI:10.1002/anie.202422707

[100] Jeon D, Kim D Y, Kim H, et al. Electrochemical evolution of Ru-based polyoxometalates into Si,W-codoped RuO_x for acidic overall water splitting. Adv Mater. 2023;36(1):2304468. DOI:10.1002/adma.202304468

[101] Chen G, Lu R, Ma C, et al. A long-range disordered RuO_2 catalyst for highly efficient acidic oxygen evolution electrocatalysis. Angew Chem Int Ed. 2024;63(50):e202411603. DOI:10.1002/anie.202411603

[102] Chen J, Qi M, Yang Y, et al. Chloride residues in RuO_2 catalysts enhance its stability and efficiency for acidic oxygen evolution reaction. Angew Chem Int Ed. 2025;64(9):e202420860. DOI:10.1002/anie.202420860

[103] Huang K, Lin C, Yu G, et al. Ru/Se-RuO_2 composites via controlled selenization strategy for enhanced acidic oxygen evolution. Adv Funct Mater. 2022;33(8):2211102. DOI:10.1002/adfm.202211102

[104] Liu L, Ji Y, You W, et al. Trace lattice S inserted RuO_2 flexible nanosheets for efficient and long - term acidic oxygen evolution catalysis. Small. 2023;19(38):2208202. DOI:10.1002/smll.202208202

[105] Yao Q, Yu Z, Chu Y-H, et al. S incorporated RuO_2-based nanorings for active and stable water oxidation in acid. Nano Res. 2022;15(5):3964-3970. DOI:10.1007/s12274-022-4081-4

[106] Xue Y, Zhao J, Huang L, et al. Stabilizing ruthenium dioxide with cation-anchored sulfate for durable oxygen evolution in proton-exchange membrane water electrolyzers. Nat Commun. 2023;14:8093. DOI:10.1038/s41467-023-43977-7

[107] He J, Chen W, Gao H, et al. Tuning hydrogen binding modes within RuO_2 lattice by proton and electron co-doping for active and stable acidic oxygen evolution. Chem Catal. 2022;2(3):578-594. DOI:10.1016/j.checat.2022.01.012

[108] Wang J, Yang H, Li F, et al. Single-site Pt-doped RuO_2 hollow nanospheres with interstitial C for high-performance acidic overall water splitting. Sci Adv. 2022;8(9):eabl9271. DOI:10.1126/sciadv.abl9271

[109] Wang J, Cheng C, Yuan Q, et al. Exceptionally active and stable RuO_2 with interstitial carbon for water oxidation in acid. Chem. 2022;8(6):1673-1687. DOI:10.1016/j.chempr.2022.02.003

[110] Shi Z, Li J, Wang Y, et al. Customized reaction route for ruthenium oxide towards stabilized water oxidation in high-performance PEM electrolyzers. Nat Commun.

2023;14:843. DOI:10.1038/s41467-023-36380-9

[111] Cao X, Qin H, Zhang J, et al. Regulation of oxide pathway mechanism for sustainable acidic water oxidation. J Am Chem Soc. 2024;146(46):32049-32058. DOI:10.1021/jacs.4c12942

[112] Lin Y, Tian Z, Zhang L, et al. Chromium-ruthenium oxide solid solution electrocatalyst for highly efficient oxygen evolution reaction in acidic media. Nat Commun. 2019;10:162. DOI:10.1038/s41467-018-08144-3

[113] Wu X, Wu J, Hu Y, et al. Multi-component and nanoporous design toward RuO_2-based electrocatalyst with enhanced performance for acidic water splitting. Small. 2024;20(45):2404019. DOI:10.1002/smll.202404019

[114] Zhu W, Song X, Liao F, et al. Stable and oxidative charged Ru enhance the acidic oxygen evolution reaction activity in two-dimensional ruthenium-iridium oxide. Nat Commun. 2023;14:5365. DOI:10.1038/s41467-023-41036-9

[115] Yuan Y, Fang H, Chen K, et al. Engineering high-density grain boundaries in $Ru_{0.8}Ir_{0.2}O_x$ solid-solution nanosheets for efficient and durable OER electrocatalysis. Adv Mater. 2025;2501607. DOI:10.1002/adma.202501607

[116] Qin Y, Yu T, Deng S, et al. RuO_2 electronic structure and lattice strain dual engineering for enhanced acidic oxygen evolution reaction performance. Nat Commun. 2022;13:3784. DOI:10.1038/s41467-022-31468-0

[117] Li Z, Sheng H, Lin Y, et al. Rutile-structured $Ru_{0.48}Mn_{0.52}O_2$ solid solution for highly active and stable oxygen evolution at large current density in acidic media. Adv Funct Mater. 2024;34(51):2409714. DOI:10.1002/adfm.202409714

[118] Liu Y, Li X, Jang H, et al. Self-limiting surface leaching stabilizes Ru-based catalysts for acidic water oxidation. Energy Environ Sci. 2025; DOI:10.1039/d4ee05220j

[119] Liu Y, Hu X, Liu C, et al. Construction of Pd-doped RuO_2 nanosheets for efficient and stable acidic water oxidation. Green Energy Environ. 2024;9(6):937-948. DOI:10.1016/j.gee.2023.12.003

[120] Liu Z, Liu H, Xue T, et al. Synergistic Sr activation and Cr buffering effect on RuO_2

electronic structures for enhancing the acidic oxygen evolution reaction. Nano Lett. 2024;24(35):10899-10907. DOI:10.1021/acs.nanolett.4c02605

[121] Hu W, Huang B, Sun M, et al. Doping Ti into RuO_2 to accelerate bridged-oxygen-assisted deprotonation for acidic oxygen evolution reaction. Adv Mater. 2024;37(3):2411709. DOI:10.1002/adma.202411709

[122] Wen Y, Liu C, Huang R, et al. Introducing Brønsted acid sites to accelerate the bridging-oxygen-assisted deprotonation in acidic water oxidation. Nat Commun. 2022;13:4871. DOI:10.1038/s41467-022-32581-w

[123] Hou L, Li Z, Jang H, et al. Electronic and lattice engineering of ruthenium oxide towards highly active and stable water splitting. Adv Energy Mater. 2023;13(22):2300177. DOI:10.1002/aenm.202300177

[124] Zou X, Li Z, Liang Q, et al. Multitasking-effect Ca ions triggered symmetry-breaking of RuO_2 coordination for acidic oxygen evolution reaction. Nano Lett. 2024;24(50):16151-16158. DOI:10.1021/acs.nanolett.4c05139

[125] Roy C, Rao R R, Stoerzinger K A, et al. Trends in activity and dissolution on RuO_2 under oxygen evolution conditions: particles versus well-defined extended surfaces. ACS Energy Lett. 2018;3(9):2045-2051. DOI:10.1021/acsenergylett.8b01178

[126] Xu J, Yang Y, Jin H, et al. Bridging gaps between lab- and fab-oriented anode design for proton exchange membrane water electrolyzers. Chem. 2025;11(1):102305. DOI:10.1016/j.chempr.2024.09.004

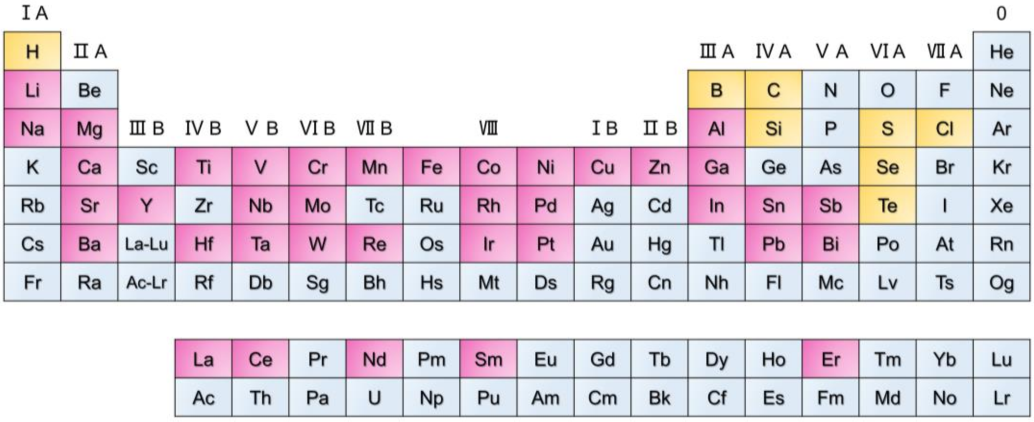

IA																	0
H	IIA											IIIA	IVA	VA	VIA	VIIA	He
Li	Be											B	C	N	O	F	Ne
Na	Mg	IIIB	IVB	VB	VIB	VIIB		VIII		IB	IIB	Al	Si	P	S	Cl	Ar
K	Ca	Sc	Ti	V	Cr	Mn	Fe	Co	Ni	Cu	Zn	Ga	Ge	As	Se	Br	Kr
Rb	Sr	Y	Zr	Nb	Mo	Tc	Ru	Rh	Pd	Ag	Cd	In	Sn	Sb	Te	I	Xe
Cs	Ba	La-Lu	Hf	Ta	W	Re	Os	Ir	Pt	Au	Hg	Tl	Pb	Bi	Po	At	Rn
Fr	Ra	Ac-Lr	Rf	Db	Sg	Bh	Hs	Mt	Ds	Rg	Cn	Nh	Fl	Mc	Lv	Ts	Og
			La	Ce	Pr	Nd	Pm	Sm	Eu	Gd	Tb	Dy	Ho	Er	Tm	Yb	Lu
			Ac	Th	Pa	U	Np	Pu	Am	Cm	Bk	Cf	Es	Fm	Md	No	Lr

Figure 1. The heteroelement doping in recently reported RuO_2-based electrocatalysts.

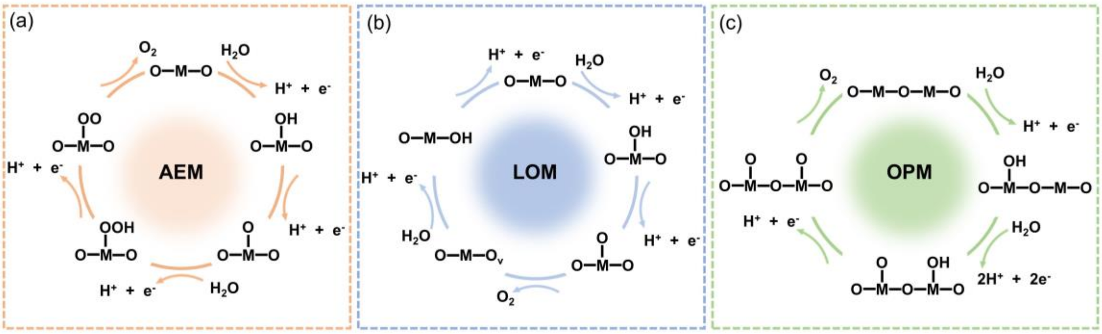

Figure 2. Schematic illustration of the OER mechanisms for metal oxide-based electrocatalysts.

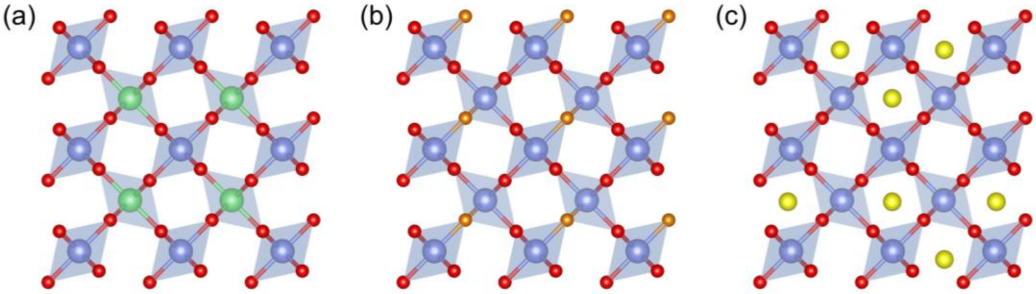

Figure 3. (a) cation doping, (b) anion doping, and (c) interstitial doping.

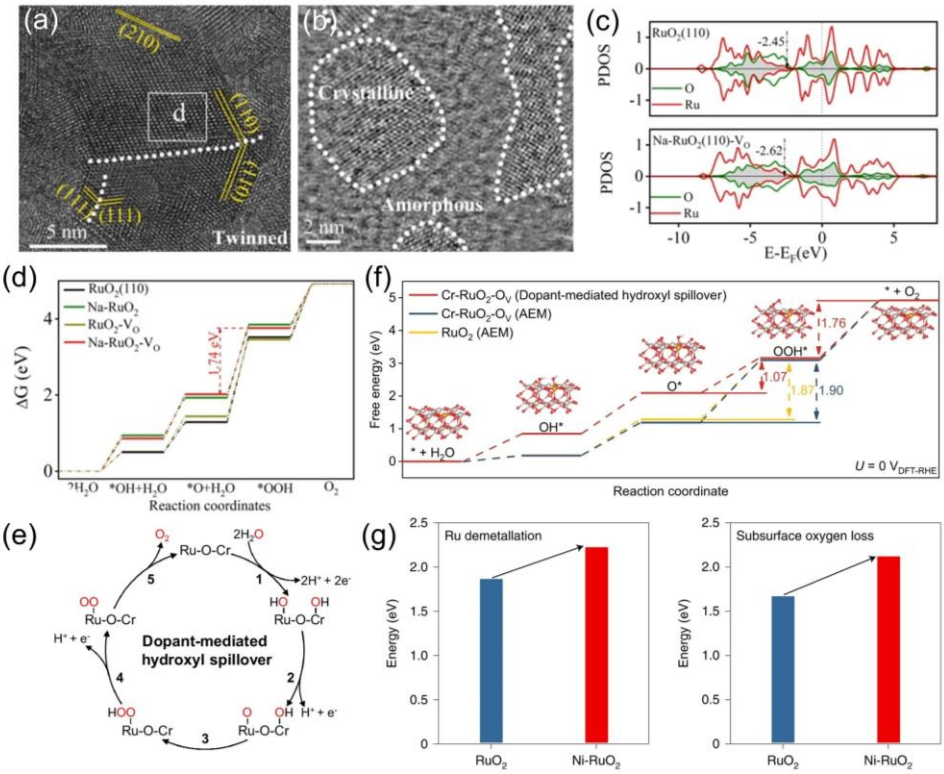

Figure 4. (a) HRTEM image and (b) atomic-resolution HAADF-STEM image of a/c-RuO_2. (c) Comparisons of free energy diagrams of OER on RuO_2, Na-RuO_2, RuO_2-V_O, and Na-RuO_2-V_O surfaces. (d) Projected density of states (PDOS) of d-bands of Ru for RuO_2 and Na-RuO_2-V_O. Reproduced with permission from [47], Copyright 2021, Wiley. (e) Schematic illustration of dopant-mediated hydroxyl spillover mechanism on $Cr_{0.2}Ru_{0.8}O_{2-x}$. (f) Calculated free energy diagrams of RuO_2 and Cr-RuO_2-O_V. Reproduced with permission from [54], Copyright 2024, Springer Nature. (g) Calculated energies cost for structural degradation of RuO_2 and Ni-RuO_2. Reproduced with permission from [59], Copyright 2023, Springer Nature.

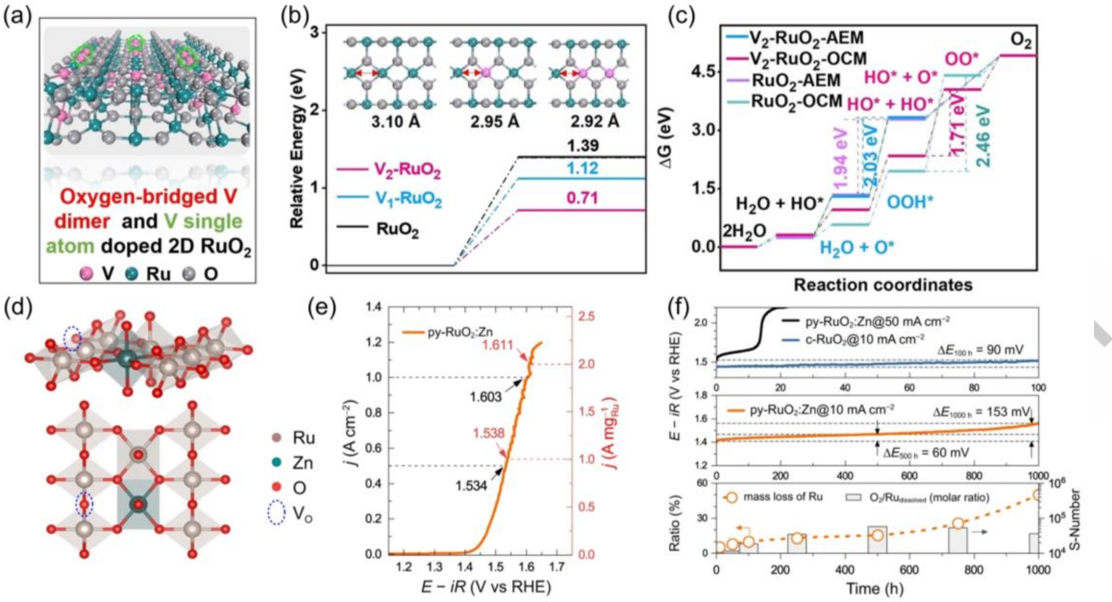

Figure 5. (a) Crystalline structure of V_n−RuO_2 (n=1 or 2). (b) Relative energies of O−O coupling on RuO_2, V_1−RuO_2 and V_2−RuO_2. (c) Free energy diagrams on the surfaces of RuO_2 and V_2−RuO_2 with different OER pathways. Reproduced with permission from [63], Copyright 2024, Wiley. (d) Schematic diagram of simulated structure of the py-RuO_2:Zn. (e) Normalized LSV curve of py-RuO_2:Zn using geometric area and Ru mass. (f) Chronopotentiometry curves of py-RuO_2:Zn and c-RuO_2 and mass loss of Ru and corresponding stability number (S-Number) on py-RuO_2:Zn during the stability test. Reproduced with permission from [65], Copyright 2023, Springer Nature.

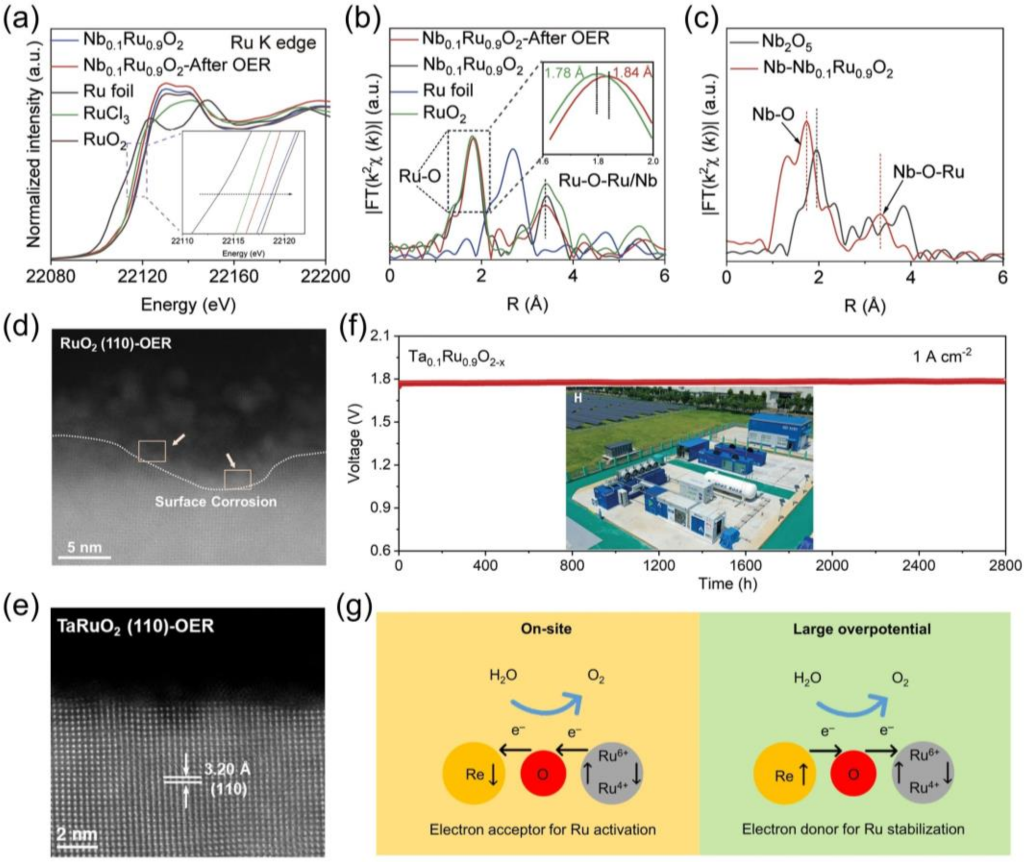

Figure 6. (a) Ru K-edge spectra, (b) Ru K-edge FT-EXAFS spectra, and (c) Nb K-edge FT-EXAFS spectra of different samples. Reproduced with permission from [58], Copyright 2023, Elsevier Inc. (d) HAADF-STEM image of RuO_2 (110) surface after OER test. (e) HAADF-STEM image of $TaRuO_2$ (110) surface after OER test. (f) Stability test of $Ta_{0.1}Ru_{0.9}O_{2-x}$-based PEMWE. Reproduced with permission from [62], Copyright 2025, American Association for the Advancement of Science. (g) Schematic illustration of the dynamic electron transfer in $Re_{0.06}Ru_{0.94}O_2$. Reproduced with permission from [60], Copyright 2023, Springer Nature.

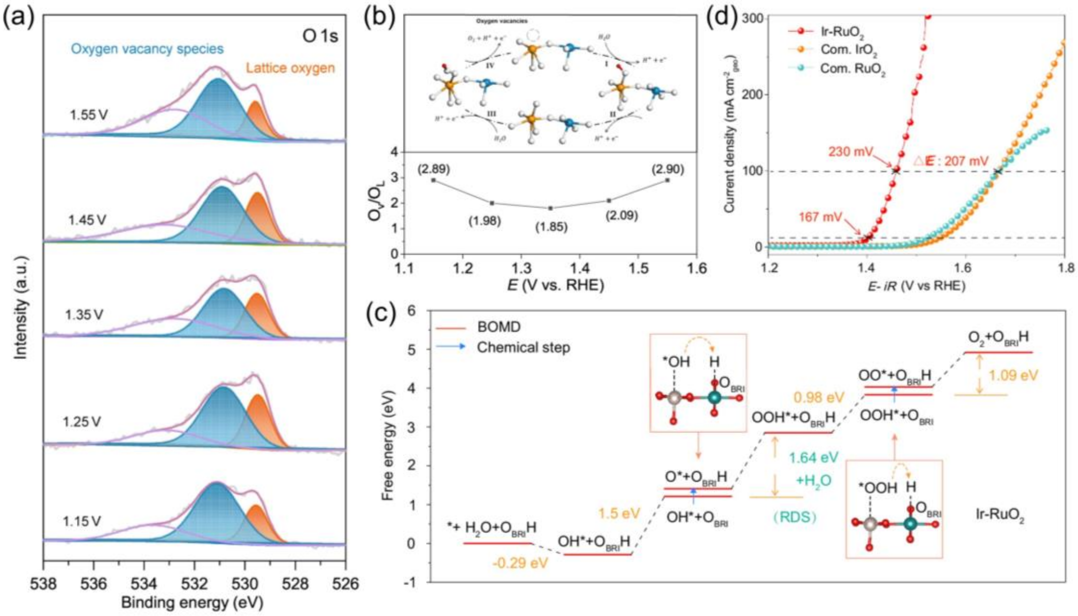

Figure 7. (a) The quasi in situ O 1s XPS spectra and (b) corresponding variation of O_V/O_L of Rh-RuO$_2$/G. Reproduced with permission from [50], Copyright 2023, Springer Nature. (c) Free energy diagram of Ir-RuO$_2$. (d) Polarization curves of Ir-RuO$_2$, commercial RuO$_2$ and IrO$_2$. Reproduced with permission from [51], Copyright 2024, Springer Nature.

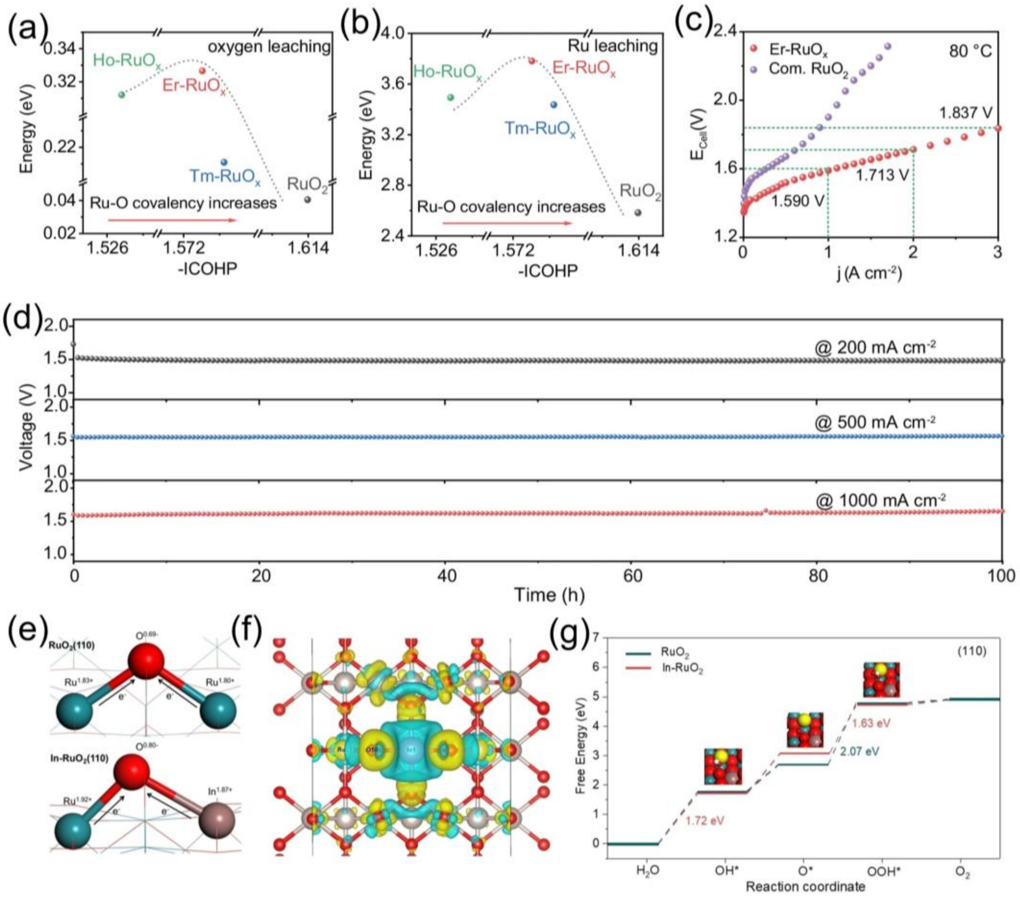

Figure 8. The formation energy of the (a) lattice oxygen and (b) Ru vacancy as a function of -ICOHP for Ln-RuO$_x$. (c) Polarization curves of the PEMWEs using Er-RuO$_x$ and commercial RuO$_2$ as anode catalysts. (d) The Chronopotentiometry curves of the PEMWE using Er-RuO$_x$ as an anode catalyst. Reproduced with permission from [71], Copyright 2024, Springer Nature. (e) The difference in electron transfer between RuO$_2$ and In−RuO$_2$. (f) Charge density difference analysis for In−RuO$_2$. (g) Free energies of the RuO$_2$ and In−RuO$_2$. Reproduced with permission from [82], Copyright 2023, Wiley.

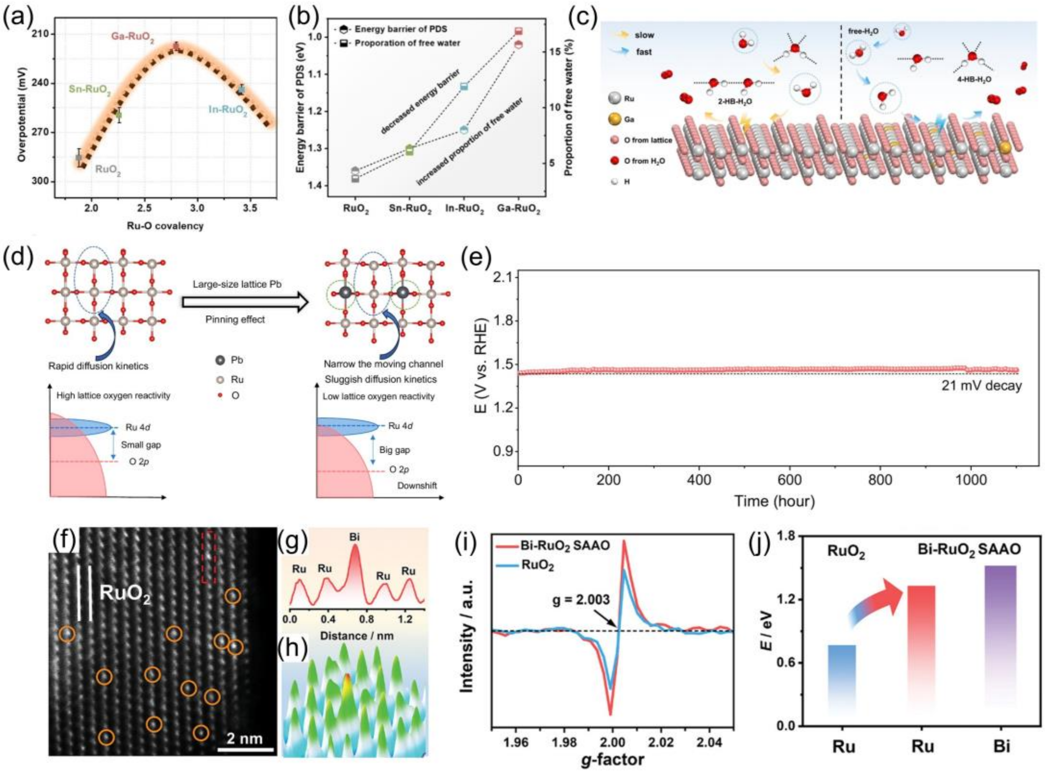

Figure 9. (a) Volcano plot of overpotential at 10 mA cm^{-2} in relation to the Ru−O covalency. (b) Calculated OER energy barrier and the proportion of free-H_2O at 1.5 V vs. RHE. (c) Schematic illustration of interfacial water splitting on the surface of RuO_2 and Ga−RuO_2. Reproduced with permission from [80], Copyright 2024, Wiley. (d) Schematic illustration of the enhanced stability caused by the pinning effect of lattice Pb. (e) Chronopotentiometry curve of Pb-RuO_2 at 10 mA cm^{-2}. Reproduced with permission from [84], Copyright 2024, Springer Nature. (f) Aberration-corrected HAADF-STEM image of Bi-RuO_2 SAAO. (g-h) the intensity profiles and 3D surface plots image corresponding to the red line in Figure f. (i) EPR spectra of Bi-RuO_2 SAAO and commercial RuO_2. (j) Calculated energies cost for structural degradation of surfaces of RuO_2 and Bi-RuO_2 SAAO. Reproduced with permission from [77], Copyright 2025, Wiley.

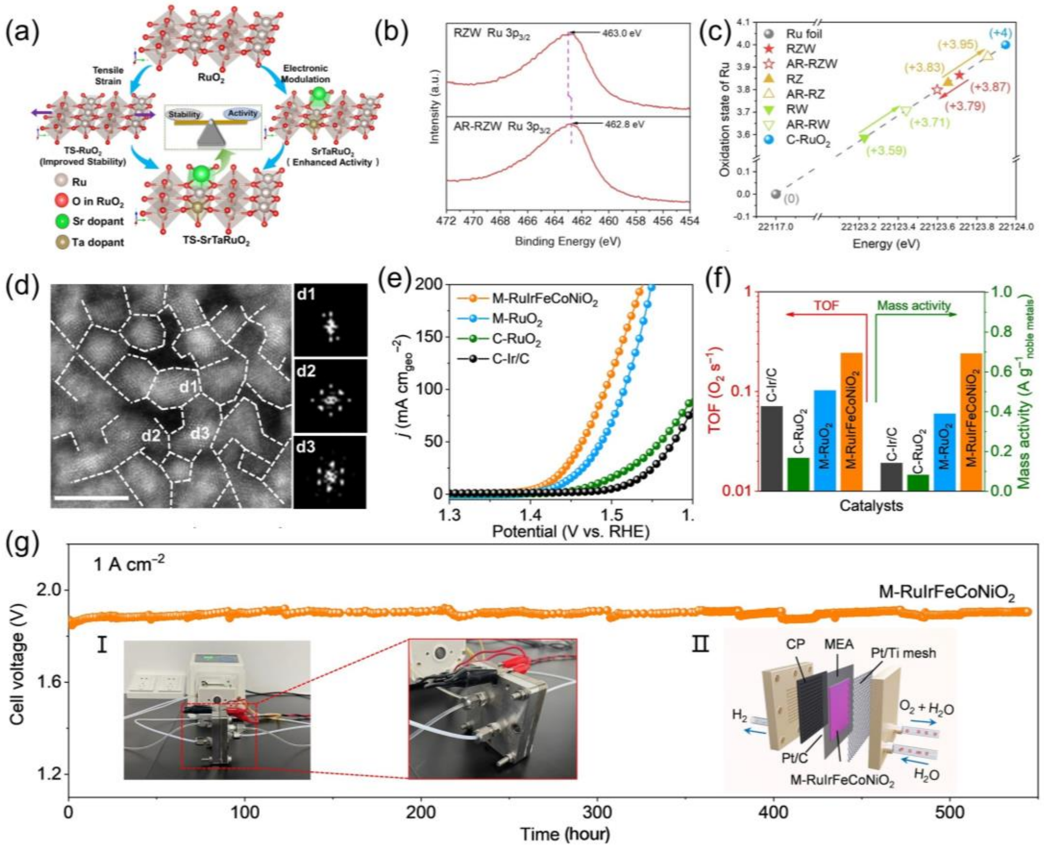

Figure 10. (a) Schematic illustration of proposed strategies for breaking stability-activity trade-off of acidic OER for TS-SrTaRuO$_2$. Reproduced with permission from [97], Copyright 2025, Springer Nature. (b) XPS Ru 3p$_{3/2}$ spectra of the RZW and AR-RZW catalysts. (c) The corresponding valence state fitting of the different samples. Reproduced with permission from [99], Copyright 2025, Wiley. (d) Aberration-corrected HAADF-STEM image of M-RuIrFeCoNiO$_2$ and corresponding fast Fourier transform patterns. (e) Polarization curves of M-RuIrFeCoNiO$_2$ and other samples. (f) Comparison of TOF and mass activities of M-RuIrFeCoNiO$_2$ and other samples at an overpotential of 300 mV. (g) Chronopotentiometry curves of M-RuIrFeCoNiO$_2$ in the PEM electrolyzer. Reproduced with permission from [91], Copyright 2023, American Association for the Advancement of Science.

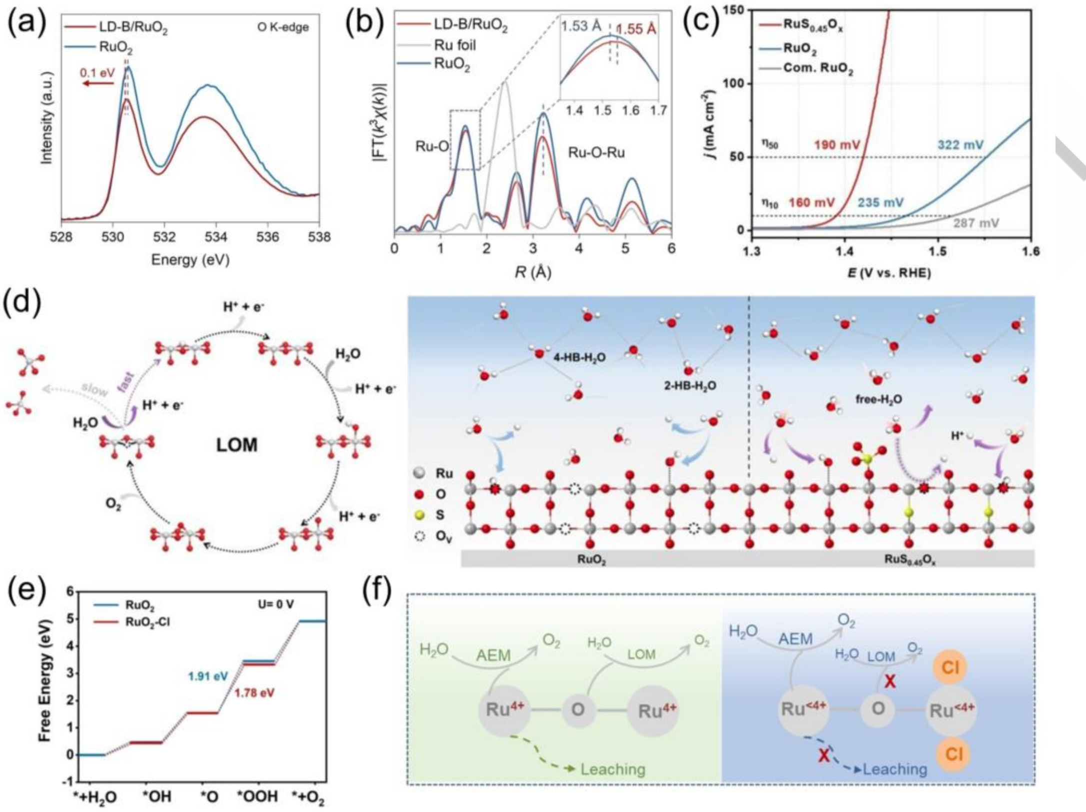

Figure 11. (a) Normalized O K-edge XAS spectra. (b) Ru K-edge FT-EXAFS spectra. Reproduced with permission from [101], Copyright 2024, Wiley. (c) LSV curves of RuS$_{0.45}$O$_x$, RuO$_2$, and commercial RuO$_2$. (d) Schematic illustration of the LOM pathway and the interfacial water molecules dynamic evolution process. Reproduced with permission from [41], Copyright 2025, Wiley. (e) Free energy diagrams of RuO$_2$-Cl and RuO$_2$ for AEM pathway. (f) Schematic illustration of structure evolution and OER mechanism transfer of pure RuO$_2$ (left) and RuO$_2$-Cl (right). Reproduced with permission from [102], Copyright 2025, Wiley.

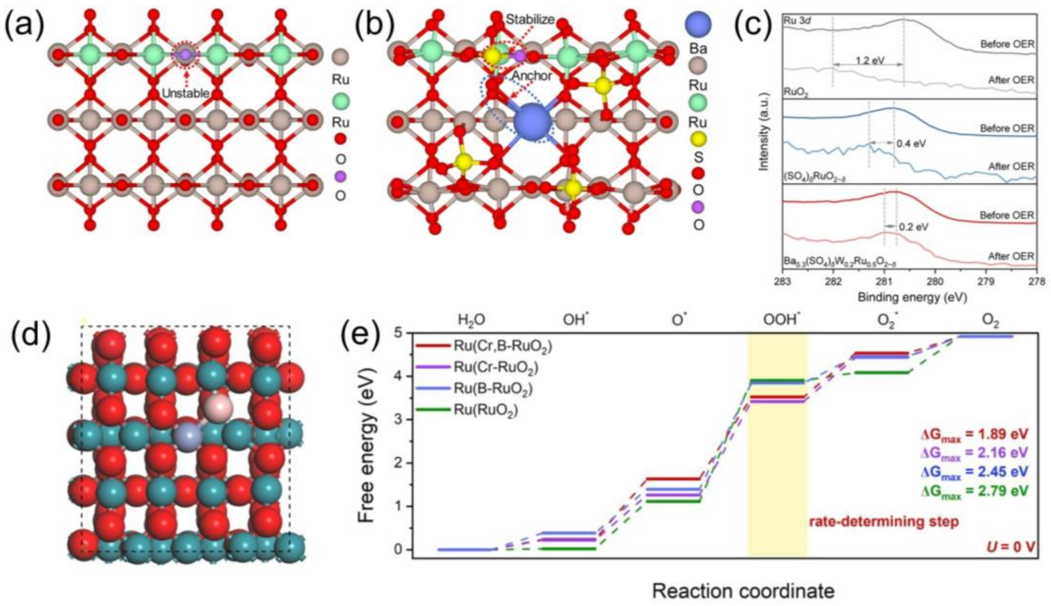

Figure 12. (a) Crystalline structure model of the RuO_2 (110) plane. (b) Crystalline structure model of Ba-anchored sulfate on the RuO_2 (110) plane. (c) High-resolution XPS spectra of Ru 3d for different samples before and after OER. Reproduced with permission from [106], Copyright 2023, Springer Nature. (d) The theoretical model of the Cr,B-RuO_2 (110) plane. (e) Free energy diagrams of different catalysts. Reproduced with permission from [43], Copyright 2024, American Chemical Society.

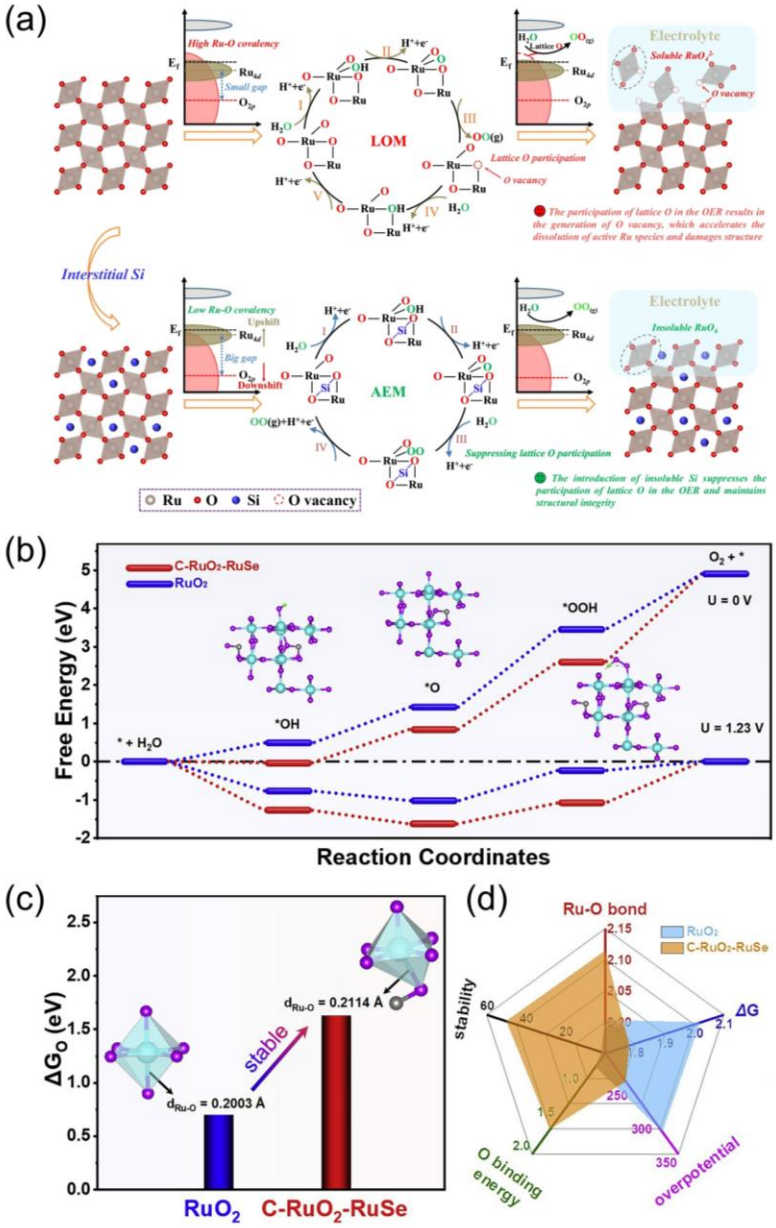

Figure 13. (a) Schematic illustration of the improved stability caused by interstitial Si doping. Reproduced with permission from [42], Copyright 2024, Springer Nature. (b) The free energy diagrams of RuO_2 and C-RuO_2-RuSe-10. (c) The dissociation energy of *O in RuO_2 and

C-RuO_2-RuSe-10. (d) Schematic illustration of the structure-activity relationship of RuO_2 and C-RuO_2-RuSe-10. Reproduced with permission from [109], Copyright 2022, Elsevier.

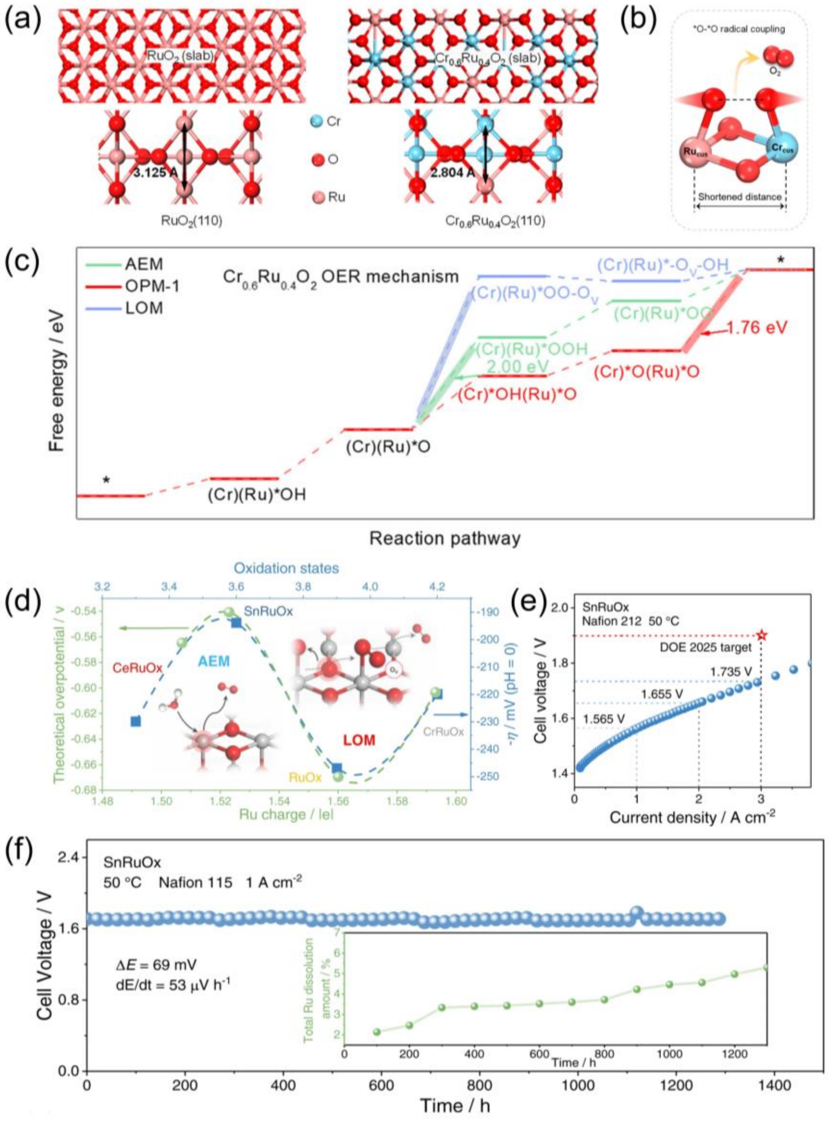

Figure 14. (a) Crystalline structure models of RuO_2 slab, $Cr_{0.6}Ru_{0.4}O_2$ slab, RuO_2 (110), and $Cr_{0.6}Ru_{0.4}O_2$ (110) facets. (b) O–O radical coupling of dual active sites. (c) Free energy diagrams of $Cr_{0.6}Ru_{0.4}O_2$ for different pathways. Reproduced with permission from [111], Copyright 2024, American Chemical Society. (d) The variation of apparent overpotential with

Ru oxidation states and the variation of the theoretical overpotential with Ru charge. (e) Polarization curve of the $SnRuO_x$-based PEMWE. (f) Chronopotentiometry curve of the $SnRuO_x$-based PEMWE. Reproduced with permission from [110], Copyright 2023, Springer Nature.

Table 1. Summary of doped RuO_2-based electrocatalysts toward acidic OER.

Classification	Catalysts	Electrolyte	Overpotential (mV) at 10 mA cm^{-2}	Stability (h)	PEMWE stability (h)	Reference
Cation doping	Mg-RuO_2 (350)	0.5 M H_2SO_4	228	30@10 mA cm^{-2}	–	[46]
	Na doped a/c-RuO_2	0.1 M $HClO_4$	205	60@10 mA cm^{-2}	–	[47]
	Ba-RuO_2	0.1 M $HClO_4$	229	250@10 mA cm^{-2}	120@10 mA cm^{-2}	[48]
	Na-RuO_2	0.1 M $HClO_4$	200	1800@10 mA cm^{-2}	25@500 mA cm^{-2} 50@300 mA cm^{-2} 80@200 mA cm^{-2}	[49]
	Rh-RuO_2/G	0.5 M H_2SO_4	161	700@50 mA cm^{-2} 500@100 mA cm^{-2}	–	[50]
	Ir-RuO_2	0.5 M H_2SO_4	167	1023@10 mA cm^{-2}	300@1A cm^{-2}	[51]
	$(RuIr)O_2$/C	0.1 M $HClO_4$	174	360@100 mA cm^{-2}	250@1A cm^{-2}	[52]
	$Cr_{0.31}Ru_{0.69}O_2$	0.5 M H_2SO_4	176	1400@10 mA cm^{-2}	2300@300 mA cm^{-2} 200@1A cm^{-2}	[53]
	$Cr_{0.2}Ru_{0.8}O_{2-x}$	0.1 M $HClO_4$	170	2000@10 mA cm^{-2}	200@1A cm^{-2}	[54]
	Cu-doped RuO_2	0.5 M H_2SO_4	188	8@10 mA cm^{-2}	–	[40]
	Mn-RuO_2	0.5 M H_2SO_4	158	10@10 mA cm^{-2}	–	[55]
	H-$Mn_{0.1}Ru_{0.9}O_2$	0.5 M H_2SO_4	169	1000@10 mA cm^{-2}	–	[56]
	$Mo_{0.15}$-RuO_2	0.5 M H_2SO_4	147	20@10 mA cm^{-2}	–	[57]
	$Nb_{0.1}Ru_{0.9}O_2$	0.5 M H_2SO_4	204	–	100@300 mA cm^{-2}	[58]
	Ni-RuO_2	0.1 M $HClO_4$	214	200@10 mA cm^{-2}	1000@200 mA cm^{-2}	[59]
	$Re_{0.06}Ru_{0.94}O_2$	0.1 M $HClO_4$	190	200@10 mA cm^{-2}	–	[60]
	Ta-RuO_2	0.1 M $HClO_4$	201	280@10 mA cm^{-2}	–	[61]
	$Ta_{0.1}Ru_{0.9}O_{2-x}$	0.5 M H_2SO_4	226	–	2800@1A cm^{-2} (25 cm × 25 cm MEA)	[62]
	V_n-RuO_2	0.1 M $HClO_4$	227	1050@10 mA cm^{-2}	–	[63]
	$ZnRuO_x$	0.5 M H_2SO_4	255	320@10 mA cm^{-2}	120@200 mA cm^{-2}	[64]
	py-RuO_2:Zn	0.5 M H_2SO_4	173	1000@10 mA cm^{-2}	–	[65]
	TE-Zn/RuO_2	0.1 M $HClO_4$	191	100@200 mA cm^{-2}	300@500 mA cm^{-2}	[66]

	Zn-doped RuO_2	0.5 M H_2SO_4	206	30@10 mA cm^{-2}	–	[67]
	$Y_{0.3}Ru_{0.7}O_2$	0.5 M H_2SO_4	170	300@10 mA cm^{-2} 200@100 mA cm^{-2}	300@0.5 A cm^{-2}	[68]
	Ce@RuO_2/CoNC	0.5 M H_2SO_4	150	1000@10 mA cm^{-2}	1000@200 mA cm^{-2}	[69]
	Ce-RuO_{2-x}	0.5 M H_2SO_4	215.1	300@10 mA cm^{-2}	–	[70]
	Er-RuO_x	0.5 M H_2SO_4	200 ± 8	200@10 mA cm^{-2}	100@1 A cm^{-2} 100@500 mA cm^{-2} 100@200 mA cm^{-2}	[71]
	La-RuO_2@TM	0.5 M H_2SO_4	162	450@100 mA cm^{-2}	120@1 A cm^{-2}	[72]
	La-doped RuO_2	0.5 M H_2SO_4	208	28@10 mA cm^{-2}	–	[73]
	$Nd_{0.1}RuO_x$	0.5 M H_2SO_4	211	25@10 mA cm^{-2}	50@10 mA cm^{-2}	[74]
	Sm-RuO_{2-x}-O_v	0.5 M H_2SO_4	217	320@10 mA cm^{-2}	–	[75]
	$RuSbO_x$	0.5 M H_2SO_4	217	150@100 mA cm^{-2}	200@200 mA cm^{-2}	[76]
	Bi-RuO_2 SAAO	0.5 M H_2SO_4	192	650@10 mA cm^{-2}	24@200 mA cm^{-2}	[77]
	$Bi_{0.15}Ru_{0.85}O_2$	0.5 M H_2SO_4	200	100@10 mA cm^{-2}	–	[78]
	Al-doped $RuIrO_x$	0.5 M H_2SO_4	178	300@100 mA cm^{-2}	60@1 A cm^{-2}	[79]
	Ga-RuO_2	0.5 M H_2SO_4	217.5	150@10 mA cm^{-2}	–	[80]
	Ga-RuO_x	0.5 M H_2SO_4	190	100@10 mA cm^{-2}	–	[81]
	In-RuO_2/G	0.5 M H_2SO_4	187	–	350@100 mA cm^{-2}	[82]
	Ru_3PbO_x	0.1 M $HClO_4$	201	72@10 mA cm^{-2}	300@100 mA cm^{-2}	[83]
	Pb-RuO_2	0.5 M H_2SO_4	188 ± 2	1100@10 mA cm^{-2}	100@1 A cm^{-2} 250@500 mA cm^{-2}	[84]
	$Sn_{0.1}$-RuO_2@NPC	0.5 M H_2SO_4	178	150@10 mA cm^{-2}	–	[85]
	Te-RuO_2	0.1 M $HClO_4$	115	50@10 mA cm^{-2}	–	[86]
	$Co_{0.2}Zn_{0.8}$@RuO_2	0.5 M H_2SO_4	150	–	100@500 mA cm^{-2}	[87]
	$Ru_{0.6}Cr_{0.2}Ti_{0.2}O_x$	0.5 M H_2SO_4	172	1100@10 mA cm^{-2}	200@100 mA cm^{-2} (0.05 M H_2SO_4)	[88]
	$InSnRuO_2$-450	0.5 M H_2SO_4	183	200@10 mA cm^{-2}	200@50 mA cm^{-2}	[89]
	$(Ru_{0.2}Ir_{0.2}Cr_{0.2}W_{0.2}Cu_{0.2})O_2$	0.5 M H_2SO_4	220	12@10 mA cm^{-2}	–	[90]
	M-$RuIrFeCoNiO_2$	0.5 M H_2SO_4	189	120@10 mA cm^{-2}	over 500@1 A cm^{-2}	[91]
	$RuIrFeCoCrO_2$	0.5 M H_2SO_4	185	1000@10 mA cm^{-2}	600@1 A cm^{-2}	[92]
	$Mg_{0.23}Ir_{0.13}Ru_{0.64}O_2$	0.5 M H_2SO_4	191	720@10 mA cm^{-2}	42@0.5 A cm^{-2}	[93]
	Na/Hf-RuO_2	0.5 M H_2SO_4	238	400@10 mA cm^{-2}	85@0.5 A cm^{-2}	[94]
	PtCo-RuO_2/C	0.1 M $HClO_4$	212.6 ± 5.3	20@10 mA cm^{-2}	24@1 A cm^{-2}	[95]
	SrRuIr	0.5 M H_2SO_4	190	1500@10 mA cm^{-2}	150@1 A cm^{-2}	[96]
	TS-$Sr_{0.1}Ta_{0.1}Ru_{0.8}O_{2-x}$	0.5 M H_2SO_4	166	1000@10 mA cm^{-2}	400@500 mA cm^{-2}	[97]
	$W_{0.2}Er_{0.1}Ru_{0.7}O_{2-\delta}$	0.5 M H_2SO_4	168	500@10 mA cm^{-2}	120@100 mA cm^{-2}	[98]
	$Ru_3Zn_{0.85}W_{0.15}O_x$	0.1 M $HClO_4$	200	4000@10 mA cm^{-2}	–	[99]
	Si,W-codoped RuO_x	0.5 M H_2SO_4	142	100@10 mA cm^{-2}	–	[100]
Anion doping	LD-B/RuO_2	0.5 M H_2SO_4	175	1200@10 mA cm^{-2}	300@250 mA cm^{-2}	[101]
	RuO_2-Cl/PtTi	0.5 M H_2SO_4	243	1200@100 mA cm^{-2}	–	[102]

				300@250 mA cm^{-2}		
	Ru/Se-RuO_2	0.5 M H_2SO_4	190	24@10 mA cm^{-2}	–	[103]
	$RuS_{0.45}O_x$	0.5 M H_2SO_4	160	1000@10 mA cm^{-2} 500@100 mA cm^{-2}	–	[41]
	Ru/S NSs-400	0.5 M H_2SO_4	219	600@10 mA cm^{-2}	300@250 mA cm^{-2}	[104]
Cation-anion dual doping	Cr, B-doped RuO_2 NFs	0.5 M H_2SO_4	219	188@1 A cm^{-2}	195@500 mA cm^{-2}	[43]
	S-$RuFeO_x$	0.1 M $HClO_4$	187	50@1 mA cm^{-2} 10@10 mA cm^{-2}	–	[45]
	S_H-RuCuO NRs/C	0.5 M H_2SO_4	231	250@10 mA cm^{-2}	–	[105]
	$Ba_{0.3}(SO_4)_{\delta}W_{0.2}Ru_{0.5}O_{2-\delta}$	0.5 M H_2SO_4	206	1000@10 mA cm^{-2}	300@500 mA cm^{-2}	[106]
Interstitial doping	75-H-RuO_2	0.5 M H_2SO_4	200	20@10 mA cm^{-2}	50@0.5 A cm^{-2}	[107]
	SS Pt-RuO_2 HNSs (with interstitial C)	0.5 M H_2SO_4	228	100@10 mA cm^{-2}	100@100 mA cm^{-2}	[108]
	C-RuO_2-RuSe-5	0.5 M H_2SO_4	212	30@10 mA cm^{-2}	–	[109]
	C-RuO_2-RuSe-10	0.5 M H_2SO_4	242	50@50 mA cm^{-2}		
	Si-RuO_2-0.1	0.1 M $HClO_4$	226	800@10 mA cm^{-2}	–	[42]
Solid solution oxides	$SnRuO_x$	0.5 M H_2SO_4	194	250@100 mA cm^{-2}	1300@1 A cm^{-2}	[110]
	$Cr_{0.6}Ru_{0.4}O_2$	0.5 M H_2SO_4	220	500@50 mA cm^{-2}	350@300 mA cm^{-2}	[111]
	$Cr_{0.6}Ru_{0.4}O_2$ (550)	0.5 M H_2SO_4	178	10@10 mA cm^{-2}	–	[112]
	FeCoNiCrTi-RuO_2	0.5 M H_2SO_4	167	200@10 mA cm^{-2}	–	[113]
	$Ru_{0.5}Ir_{0.5}O_2$	0.5 M H_2SO_4	151	618.3@10 mA cm^{-2}	255@200 mA cm^{-2}	[114]
	$Ru_{0.8}Ir_{0.2}O_x$	0.5 M H_2SO_4	189	100@10 mA cm^{-2}	1000@500 mA cm^{-2}	[115]
	$Li_{0.52}RuO_2$	0.5 M H_2SO_4	156	70@10 mA cm^{-2}	–	[116]
	$Ru_{0.48}Mn_{0.52}O_2$	0.5 M H_2SO_4	154	50@100 mA cm^{-2}	–	[117]
	$Ru_{0.2}Mn_{0.8}O_2$	0.5 M H_2SO_4	214	50@10 mA cm^{-2}	100@200 mA cm^{-2}	[44]
	$Ru_{0.5}Mn_{0.5}O_2$	0.5 M H_2SO_4	166	2500@10 mA cm^{-2}	600@200 mA cm^{-2}	[118]
	$Pd_{0.08}Ru_{0.92}O_2$	0.5 M H_2SO_4	204	19.44@10 mA cm^{-2}	130@200 mA cm^{-2}	[119]
	$Ru_3Cr_1Sr_{0.175}$	0.1 M $HClO_4$	214	300@10 mA cm^{-2}	–	[120]
	$RuTiO_x$	0.5 M H_2SO_4	198	1400@50 mA cm^{-2}	100@0.5 A cm^{-2}	[121]
	$Ru_5W_1O_x$	0.5 M H_2SO_4	227	550@10 mA cm^{-2}	–	[122]
	$Ru_{0.85}Zn_{0.15}O_{2-\delta}$	0.5 M H_2SO_4	190	50@10 mA cm^{-2}	–	[123]

Biographical_note_for_all_authors

Yihao Zheng received his B.S. degree from South China Agricultural University in 2019, and then worked as a research assistant for another three years. Currently, he is a Ph.D. candidate under the supervision of Prof. Huaiyu Shao and Prof. Xinchun Yang at University of Macau and Shenzhen Institute of Advanced Technology, Chinese Academy of Sciences. His research interests focus on metal oxide electrocatalysts for water splitting and nitrate reduction.

Tao Zhou, Ph.D., is an Assistant Researcher and Pengcheng Peacock Plan (Class C) Talent in Shenzhen. Her research focuses on nanogenerators, wearable flexible sensing devices, life cycle assessment, and carbon neutrality strategies. She has published 21 SCI-indexed papers in prestigious journals including ACS Nano and

Nano Energy, including 5 as first/co-first author, with total citations exceeding 1,300 (single paper highest: 270+). She has obtained or filed 15 patents, including national invention patents and PCT applications, has delivered more than 6 presentations at top-tier international conferences (e.g., NENS, NGPT).

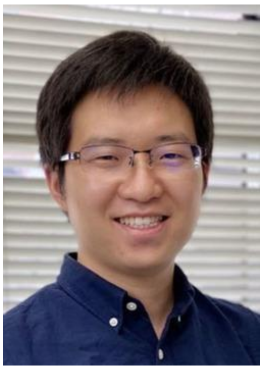

Quan Zhang is currently a professor at the College of Materials Science and Engineering, Donghua University. He received his Ph.D. in 2018 at Kyoto University under the supervision of Prof. Hiroshi Kitagawa. From 2018 to 2023, he worked as a postdoctoral assistant at Kyoto University, and National University of Singapore. His main research interests are the preparation of metal and alloy nanomaterials and catalytic applications.

Haixin Guo is a professor at the Agro-Environmental Protection Institute, Ministry of Agriculture and Rural Affairs (Tianjin, China). She obtained her M.S. Degree in

Environmental Engineering from Nankai University in China and her Doctor of Philosophy in Environmental Science at Tohoku University (Japan). She has published more than 60 scientific papers and has research interests in sustainable catalyst development, hydrothermal reactions including carbonization, solvothermal and mechanochemical pretreatment of biomass, and conversion of biomass into chemicals and biofuels.

Baofu Ding is currently a Grade-One associate professor at the Institute of Technology for Carbon Neutrality, Shenzhen Institute of Advanced Technology, Chinese Academy of Sciences, and a research Associate Professor at Shenzhen University of Technology. He received his PhD from Fudan University in 2009, and has worked as a postdoctoral fellow in the University of Hong Kong, Edith Cowan University in Australia, and as a senior research scientist in Shenzhen International Graduate School of Tsinghua University. His main research interests are the controllable preparation of low-dimensional materials and their unique applications.

Huaiyu Shao is an associate professor at the Institute of Applied Physics and Materials Engineering, University of Macau. He obtained B.Sc. (2000) and Ph.D. (2005) degrees from Peking University and worked as a postdoc at

National Institute of Advanced Industrial Science and Technology, Japan from 2005 to 2009 and at Max-PlanckInstitut für Kohlenforschung, Germany from 2009 to 2011. Before the position in Macau, he was an assistant professor at International Institute for Carbon-Neutral Energy Research (WPI-I2CNER) at Kyushu University. His research interests include electrode materials, silicon-based anode materials, electrode pre-lithiation, and solid-state batteries.

Xinchun Yang is a principal investigator of the Shenzhen Institutes of Advanced Technology (SIAT), Chinese Academy of Sciences (CAS). He received his Ph.D. in Chemical Science and Engineering at Kobe University in 2018, and then moved to the National Institute of Advanced Industrial Science and Technology (AIST), Korea

Advanced Institute of Science and Technology (KAIST) and the Ulsan National Institute of Science and Technology (UNIST) for postdoctoral researches from May 2018 to Dec. 2021, respectively. He joined SIAT in Jan. 2022 and established the SIAT-Clean Energy International Joint Laboratory. His research focuses on the synthesis of nanoporous materials and their hydrogen energy applications, especially, in the controllable construction and regulation of confined metal clusters using porous organic cages for ammonia-hydrogen energy applications.

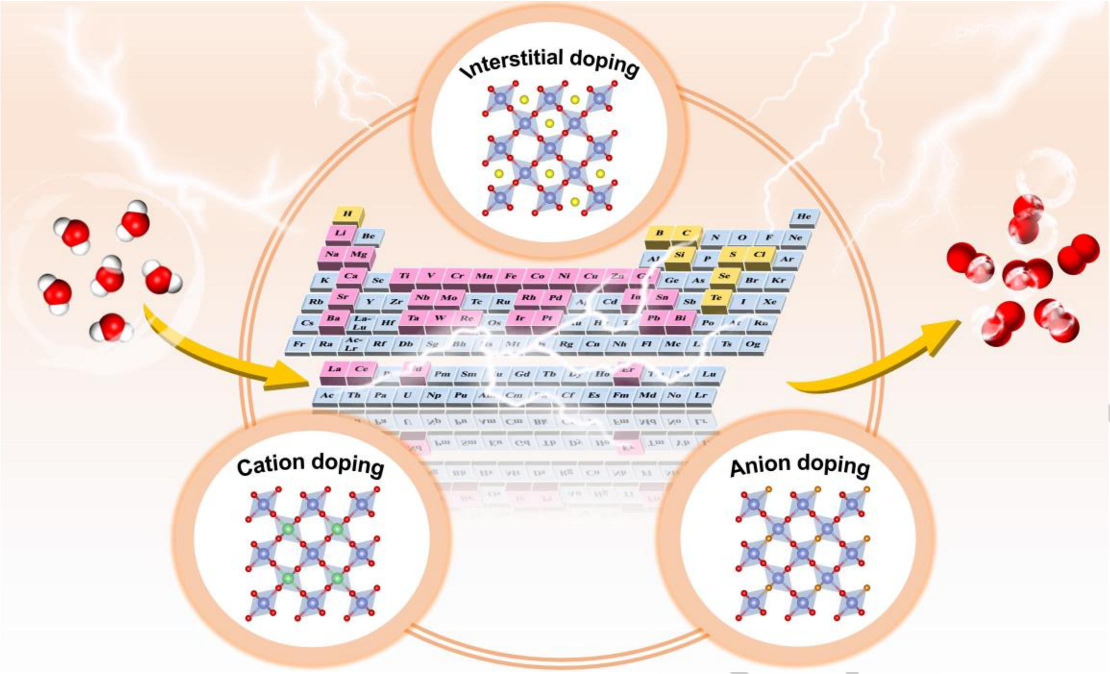

Graphical abstract